





## Structure and electronic tunability of acene alkylamine based layered hybrid organic-inorganic perovskites from first principles

Ruyi Song <sup>1</sup>, Chi Liu,<sup>1</sup> Yosuke Kanai <sup>2,3</sup>, David B. Mitzi <sup>1,4</sup> and Volker Blum <sup>1,4,\*</sup>

<sup>1</sup>Department of Chemistry, Duke University, Durham, North Carolina 27708, USA

<sup>2</sup>Department of Chemistry, University of North Carolina, Chapel Hill, North Carolina 27599, USA

<sup>3</sup>Department of Physics and Astronomy, University of North Carolina, Chapel Hill, North Carolina 27599, USA

<sup>4</sup>Thomas Lord Department of Mechanical Engineering and Materials Science, Duke University, Durham, North Carolina 27708, USA



(Received 15 March 2023; accepted 13 July 2023; published 2 August 2023)

Twelve layered hybrid organic-inorganic perovskites combining oligoacene derivatives [phenylmethylammonium (PMA), naphthylmethylammonium (NMA), anthrylmethylammonium (AMA), and tetrylmethylammonium (TMA)] and lead halides ( $\text{Cl}^-$ ,  $\text{Br}^-$ , and  $\text{I}^-$  anions) are investigated by first-principles density functional theory (DFT), showing broad, rational tunability of band gap, quantum well type, and spin-dependent energy band properties. Six compounds are known from previous syntheses and are used to devise a computational search space for likely low-energy structures. Among the six known compounds, a refined structure is identified for  $(\text{NMA})_2\text{PbCl}_4$  and a new, lower-energy structure is suggested for  $(\text{AMA})_2\text{PbCl}_4$ . The DFT based search methodology is next applied to predict the likely structures for the six unknown compounds. Computationally predicted energy levels for all 12 compounds from spin-orbit coupled hybrid DFT reveal tunable type I quantum well alignments, with frontier orbitals located on the inorganic component, on the organic component, or on both, as controlled by cation and anion selection. Several structures spontaneously break local and global inversion symmetry, causing strong spin splitting of the conduction bands [up to 0.12 eV for  $(\text{PMA})_2\text{PbCl}_4$ ] and showing potential for spin-dependent transport properties and future spintronic and tunable chiroptical applications.

DOI: [10.1103/PhysRevMaterials.7.084601](https://doi.org/10.1103/PhysRevMaterials.7.084601)

### I. INTRODUCTION

The three-dimensional (3D) hybrid organic-inorganic perovskites (HOIPs) have attracted significant attention in the areas of photovoltaics (PV) and optoelectronics in the past decade [1–3]. For instance, the record certified power conversion efficiency of laboratory PV devices based on 3D HOIPs was reported to be 25.7%, certified by the National Renewable Energy Laboratory in June 2022 [4]. Although early work highlighted the promise and diversity of HOIPs for wide-ranging applications [5], rapid advances in the PV space have spurred the widespread recognition of their potential as low-cost processing materials for other applications in the semiconductor and/or optoelectronics space, such as laser sources, light-emitting diodes (LEDs), photodetectors, photocatalysts, and spintronic devices [6–17]. Layered HOIPs, called two-dimensional (2D) HOIPs because of the two-dimensional connectivity of their inorganic component, have higher demonstrated stability than some 3D HOIPs [18–20]. Additionally, the greatly increased space of organic cations that can be incorporated into the layered framework offers significantly enhanced tunability compared with the restricted space afforded by a traditional 3D interconnected perovskite lattice [21]. In general, band gaps of 2D HOIPs (when derived from the inorganic component) are higher than the range considered optimal for PV, but even in 2D HOIPs, organic

semiconductor cations that enhance PV-related functionality may be of interest. For example, a widely pursued paradigm relates to singlet fission [22], demonstrated for pentacene materials [23], which is one potential route to enhance the carrier counts produced by a PV material beyond the thermodynamic limit. Employing acenes in layered HOIPs is therefore an intriguing idea and has long been pursued for naphthalene and anthracene [24–26]. Tetracene has also been investigated, e.g., as a surface modification of 3D perovskites [27]. In a different potential application route, the crystal structures of several past-reported acene HOIPs spontaneously break inversion symmetry (IS) [25,26,28]. This inversion asymmetry, when coupled with the strong relativistic spin-orbit coupling (SOC) of heavy cations such as  $\text{Pb}^{2+}$ , gives rise to energy bands with distinct spin expectation values and, thus, properties of potential interest for chiroptics and spintronics [15,29–32].

The purpose of this paper is to comprehensively assess the electronic properties of a class of 12 oligoacene based 2D lead halide HOIPs, including six experimentally known compounds and six compounds that have not yet been realized, by a first-principles computational analysis. Early work on oligoacene based 2D HOIPs targeted copper halides [33,34] in the context of their magnetic properties. The first published synthesis of a lead halide 2D HOIP based on oligoacene derivatives goes back to  $(\text{C}_6\text{H}_5(\text{CH}_2)_2\text{NH}_3)_2\text{PbCl}_4$  and  $(\text{C}_6\text{H}_5(\text{CH}_2)_2\text{NH}_3)_2\text{PbI}_4$ , reported by Calabrese *et al.* in 1991 [35]. This pioneering work was followed by the investigation of the strong

\*volker.blum@duke.edu

TABLE I. Experimentally reported space groups of the 2D HOIP material space investigated in this paper, as well as an indication (in parentheses) if the reported structure is globally inversion symmetric (IS) or inversion asymmetric (IA, i.e., the space group does not include inversion symmetry). PMA, NMA, AMA, and TMA represent the organic cations phenylmethylammonium, naphthylmethylammonium, anthrylmethylammonium, and tetrylmethylammonium, respectively. The abbreviation “n.y.s.” denotes compounds that are not yet synthesized experimentally to the authors’ knowledge and for which computational predictions are included in this paper.

Halogen	Organic cation			
	PMA	NMA	AMA	TMA
Cl	$Cmc2_1$ (IA) [28]	$Pbam$ (IS) [24]	$Fmm2$ (IA) [25]	n.y.s.
Br	$Cmc2_1$ (IA) [26]	$Cmc2_1$ (IA) [26]	n.y.s.	n.y.s.
I	$Pbca$ (IS) [52]	n.y.s.	n.y.s.	n.y.s.

photoluminescence of the HOIPs based on oligoacenes (containing one or two linearly conjugated acene rings and a  $-CH_2NH_3^+$  or  $-C_2H_4NH_3^+$  tail) [26,36–41]. Furthermore, Kagan *et al.* demonstrated the application of  $(C_6H_5(CH_2)_2NH_3)_2SnI_4$  as the conducting channel in spin-coated thin film field-effect transistors [42]. Ema *et al.* reported energy transfer from the excitons located on the inorganic component to the triplet states of the organic molecules in 2D HOIPs based on naphthalene and lead bromide [43], demonstrating a potential for novel optoelectronic devices by coupling of different types of excitons in the organic and inorganic components [43]. Li *et al.* demonstrated room-temperature electroluminescence from light-emitting diodes based on  $(C_6H_5NH_3)_2PbI_4$  [44]. Braun and Frey characterized the first anthryl based 2D HOIP [25]. However, solubility differences between large organics and inorganic salts limit the applicability of traditional solution processing methods to readily achieve complex oligoacene based 2D HOIPs. Despite the significant potential for further, rationally tunable hybrid semiconductors in this family of materials, the full space of lead halide (chloride, bromide, iodide) 2D HOIPs with large oligoacene based cations has therefore not yet been experimentally explored.

In this paper, we use a computational approach to explore the compound space of acene lead halide based 2D HOIPs formed by phenylmethylammonium (PMA), naphthylmethylammonium (NMA), anthrylmethylammonium (AMA), and tetrylmethylammonium (TMA) as oligoacene based cations and chloride, bromide, and iodide as the halide anions, resulting in the 12 materials listed in Table I. For each material, Table I reports the experimental space group, if known, and whether it is inversion symmetric (IS) or inversion asymmetric (IA). Based on the structural characteristics of the six previously synthesized 2D HOIPs in Table I, we reassess and/or predict the structures of all 12 oligoacene based 2D HOIPs by semilocal density functional theory (DFT) [45] including a dispersion energy correction [46] and we predict the electronic and spin properties of their band structures based on spin-orbit coupled hybrid DFT [47–49]. Large organic molecules, when incorporated into the 2D inorganic framework, allow for many degrees of freedom and complex interactions between organic and inorganic components, thus rendering the prediction of their structure challenging by computational means. We therefore determine likely structures for known and unknown oligoacene based HOIPs from first principles by exploring a set of structure prototypes based on features of the experimentally known structures. Using this set

of structures, we show that we can identify the experimentally known compounds and make plausible predictions for the ones that have, to our knowledge, not yet been synthesized experimentally. As shown below, we confirm the structures of four experimentally known compounds, i.e.,  $(PMA)_2PbCl_4$ ,  $(PMA)_2PbBr_4$ ,  $(PMA)_2PbI_4$ , and  $(NMA)_2PbBr_4$ . For  $(NMA)_2PbCl_4$ , we provide a structure model that resolves a disordered representation of the organic molecules in the experimental structure [24]. For  $(AMA)_2PbCl_4$ , we suggest a structure with significantly lower energy than the earlier experimental report [25]. We then predict the atomic structures for the as-yet unexplored compounds  $[(NMA)_2PbI_4, (AMA)_2PbBr_4, (AMA)_2PbI_4, (TMA)_2PbCl_4, (TMA)_2PbBr_4, \text{ and } (TMA)_2PbI_4]$ , as well as the energy band structures, band edges, and quantum well types of all 12 compounds. Motivated by our recent discovery of a simple structural descriptor of the relationship between structural asymmetry and spin splitting in 2D HOIPs with chiral organic cations [50,51], we also investigate frontier band spin splitting in the oligoacene based 2D HOIPs, connected to local and global inversion symmetry breaking that arises already in some experimentally reported structures  $[(PMA)_2PbCl_4, (PMA)_2PbBr_4, (NMA)_2PbBr_4, \text{ and } (AMA)_2PbCl_4]$ . By “local inversion symmetry breaking” we refer to situations in which the inversion symmetry about a particular inorganic layer is broken, even if the global space group of the crystal contains inversion symmetry but with an inversion center away from the inorganic layer [30]. In contrast, global inversion symmetry breaking refers to scenarios in which the reported space group itself does not contain inversion symmetry. In either case, a locally well-defined spin texture can arise in the band structure of oligoacene based 2D HOIPs, offering a potential future pathway to manipulate the spin properties of electronic carriers in the respective compounds.

## II. COMPUTATIONAL DETAILS

All DFT calculations are performed using the all-electron numeric atom-centered orbital based code FHI-AIMS [49,53–57]. The lattice parameters and in-cell atomic coordinates are fully relaxed for all investigated compounds (with residual forces on atoms and lattice vectors below  $5 \times 10^{-3}$  eV/Å), using the semilocal Perdew-Burke-Ernzerhof (PBE) exchange-correlation (XC) functional [45] together with the Tkatchenko-Scheffler (TS) pairwise dispersion scheme [46]. FHI-AIMS’s “intermediate” numerical defaults are employed. Unit cells are chosen to contain two  $PbX_6^{4-}$  octahedra per

inorganic layer and two inorganic layers each, referred to as  $c(2 \times 2) \times 2$  unit cells (see, e.g., Fig. S1(a) in the Supplemental Material [58] for an example).  $k$ -point grids of  $2 \times 5 \times 5$  are used to sample the Brillouin zone of each compound, where the “2” direction is perpendicular to the inorganic planes of the 2D HOIP. In order to ensure comparable  $k$  paths in band structure calculations, we always designate the  $a$  axis to be the stacking direction, even though crystallographic conventions for some of the experimental space groups might suggest a different lattice direction as the stacking direction. In past work, we have extensively validated the suitability of this general choice of computational settings and level of theory for the prediction of the structure of 3D and complex layered HOIPs, e.g., in the Supplemental Material of Ref. [59], supported by later experiment-theory comparisons in a number of other studies [17,60–64] and a summary in Supplemental Table 4.2 of Ref. [65]. One of these studies includes the experimental and computational resolution of a subtle structural difference in molecular orientation, i.e., the rotationally disordered stacking of perovskite layers [62]. While we are well aware of the potential relevance of more-refined dispersion treatments than the TS approach in complex molecular systems [66,67], our past experience with hybrid perovskites suggests that the DFT-PBE+TS level of theory is suitable for the structural predictions made for HOIPs in this paper.

For energy band structure and spin splitting calculations, the Heyd-Scuseria-Ernzerhof (HSE06) hybrid XC functional [47,48] with non-self-consistent second-variational SOC [49] was employed. FHI-AIMS’s “intermediate” numerical settings and  $3 \times 4 \times 4$   $k$ -point grids were used. In Ref. [68], the second-variational SOC scheme [49] was benchmarked against a four-component method, showing an accuracy of  $\sim 0.2$  eV for the heavily relativistic  $6p$  orbitals of Pb (compared with changes of the order of  $\sim 1$  eV if SOC were omitted altogether). The exchange mixing parameter of the HSE06 functional,  $\alpha$ , was set to 25%, and the screening parameter  $\omega$  was fixed at  $0.11 \text{ bohr}^{-1}$  [48], following the original suggestion of Krukau *et al.* [69]. This parametrization of the HSE06 functional predicts fundamental gap values with predictive accuracies of several tenths of an eV, in line with broader assessments of semiconductors in the band gap range relevant for this work [70–72]. For 2D HOIPs, high-precision experimental fundamental gap values are scarce, since they are often inferred from optical data with uncertain magnitudes of exciton binding energies. In the case of the very well studied hybrid perovskite phenethylammonium lead iodide,  $(\text{C}_6\text{H}_5(\text{CH}_2)_2\text{NH}_3)_2\text{PbI}_4$ , the present parametrization of DFT-HSE06+SOC underestimates the experimentally inferred fundamental gap of 2.65–2.68 eV [73] by about 0.6 eV, i.e., at the lower end of the expected accuracy [70–72]. In this material, the exciton binding energy amounts to around 0.26 eV at room temperature [73]. In the case of strong contributions from the organic moiety to optical spectra, however, additional and more complex excitonic and vibronic contributions [40,43,74] further complicate the extraction of fundamental gap values from optical experimental data. While one could reparametrize the DFT-HSE06+SOC functional to match, e.g., the system-specific gap of  $(\text{C}_6\text{H}_5(\text{CH}_2)_2\text{NH}_3)_2\text{PbI}_4$ , it is not clear if and how much the predictive accuracy for unknown compounds would

be improved, but qualitative comparisons with past results for other compounds would become more difficult. We therefore here retain the original Krukau suggestion for the HSE06 parameters, which we have successfully used to interpret electronic properties from 2D HOIPs in past work of our groups [59–61,73] as well.

Regarding the absolute energetic positions of optical features (which include excitonic effects that are formally not captured by DFT-HSE06+SOC), much more expensive, higher-level many-body approaches would be needed for a high-accuracy computational assessment. Interestingly, a recent study of  $(\text{PMA})_2\text{PbBr}_4$  and  $(\text{NMA})_2\text{PbBr}_4$  using the higher-level Bethe-Salpeter equation (BSE) based on  $GW$  quasiparticle energies still reports an underestimation of the experimental absorption onset by 0.5–0.6 eV by calculated values [75]. However, in past work [50,59,60,62,63,73,76], we have found that the prospects are better for qualitatively correct predictions of the quantum-well-like *alignment* of frontier energy levels (i.e., energy differences) between conjugated organic and lead halide inorganic components of 2D HOIPs, even by just interpreting DFT-HSE06+SOC energy band structures. Several of these studies demonstrate correct band alignment predictions to within a few tenths of an eV at most, for cases in which close valence band or highest occupied molecular orbital (HOMO) or conduction band or lowest unoccupied molecular orbital (LUMO) alignments are substantiated by detailed spectroscopic experiments [59,60,76]. One possible reason for this agreement is error cancellation; that is, qualitatively similar systematic errors due to DFT-HSE06+SOC and neglected excitonic effects are present in both the organic and inorganic components of the 2D HOIPs, and these errors cancel in energy differences. Given this past experience, we use DFT-HSE06+SOC energy band structures to predict the quantum well character of each acene based 2D HOIP considered in this paper as well.

### III. RESULTS AND DISCUSSION

#### A. Initial structure prototypes from features of experimentally resolved compounds

As a first step, we describe the construction of a set of 13 structure prototypes used for total-energy calculations in this paper. These prototypes are employed to computationally identify the likely structure of each of the six compounds in Table I that have not yet been synthesized. Additionally, the same prototypes are applied to provide a computational check of the experimental structure assignments of the six known compounds indicated in Table I, which are shown in Fig. 1. The 13 structure prototypes are based on structural degrees of freedom that are present in or compatible with the six experimentally known methylammonium acene lead halide compounds. As shown along with Fig. 2, eight of the 13 structure prototypes follow from  $2^3$  combinations of three structure elements derived from the five known compounds that show no disorder in their experimentally assessed organic layers [Figs. 1(a)–1(c), 1(e), and 1(f)]. The five remaining structure prototypes, described along with Fig. 3, follow from creating ordered structure models that are compatible with the disorder in the experimental structure assessment of  $(\text{NMA})_2\text{PbCl}_4$



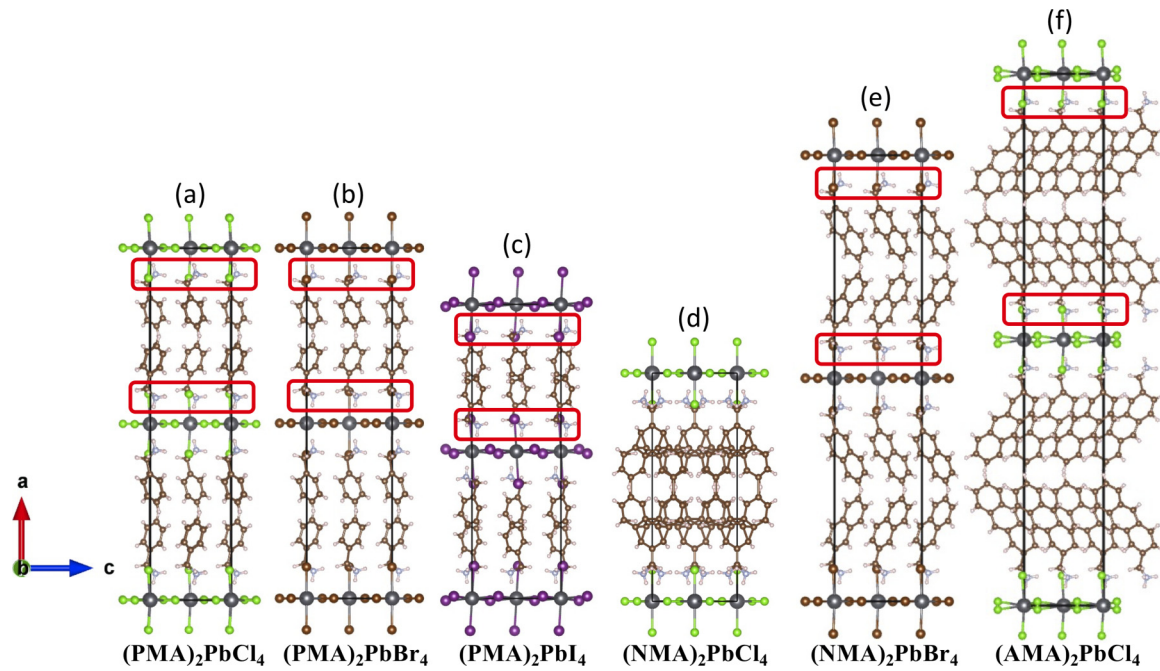


FIG. 1. Side views of the experimental structures: (a)  $(PMA)_2PbCl_4$  [28], (b)  $(PMA)_2PbBr_4$  [26], (c)  $(PMA)_2PbI_4$  [52], (d)  $(NMA)_2PbCl_4$  [24], (e)  $(NMA)_2PbBr_4$  [26], and (f)  $(AMA)_2PbCl_4$  [25]. The  $a$  axis is chosen to be oriented along the stacking direction, and unit cells are aligned based on the positions and orientations of the ammonium tails above the inorganic middle layer (marked by red outlines). The experimentally obtained  $(NMA)_2PbCl_4$  unit cell has only one organic cation layer with superpositions of organic cations in the original diffraction analysis [24]. Distinct organic cation positions in two layers are resolved by computational analysis in this paper.

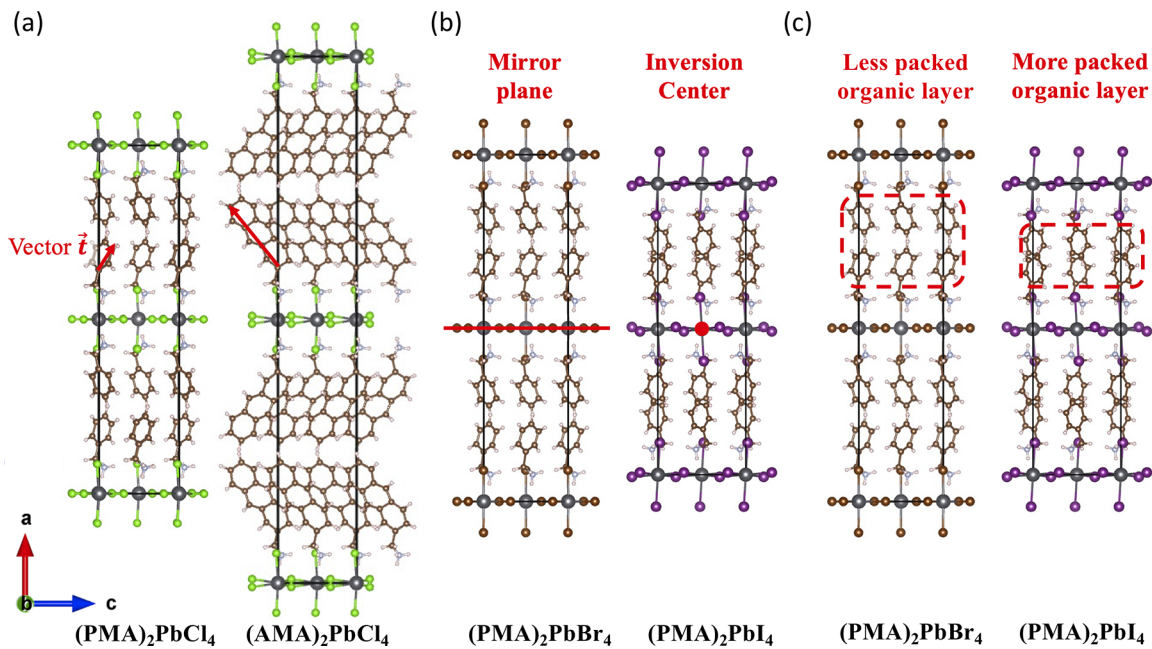


FIG. 2. Geometric degrees of freedom derived by inspecting the five experimentally known compound structures of  $(PMA)_2PbCl_4$ ,  $(PMA)_2PbBr_4$ ,  $(PMA)_2PbI_4$ ,  $(NMA)_2PbBr_4$ , and  $(AMA)_2PbCl_4$ . (a) Tilting direction of the organic rings with respect to the  $c$  direction (see text), exemplified by side views of  $(PMA)_2PbCl_4$  and  $(AMA)_2PbCl_4$  along the  $b$  axis. Red arrows show the tilting vectors  $\vec{t}$ . (b) Side views of  $(PMA)_2PbBr_4$  and  $(PMA)_2PbI_4$  along the  $b$  axis, illustrating the different symmetry elements connecting the upper and lower organic layers (mirror plane or inversion center). (c) Side views of  $(PMA)_2PbBr_4$  and  $(PMA)_2PbI_4$  along the  $b$  axis, showing less densely packed (in the vertical direction) and more densely packed organic layers along the stacking direction. A total of eight ( $2^3$ ) structure prototypes are constructed from different combinations of the degrees of freedom shown in (a)–(c).

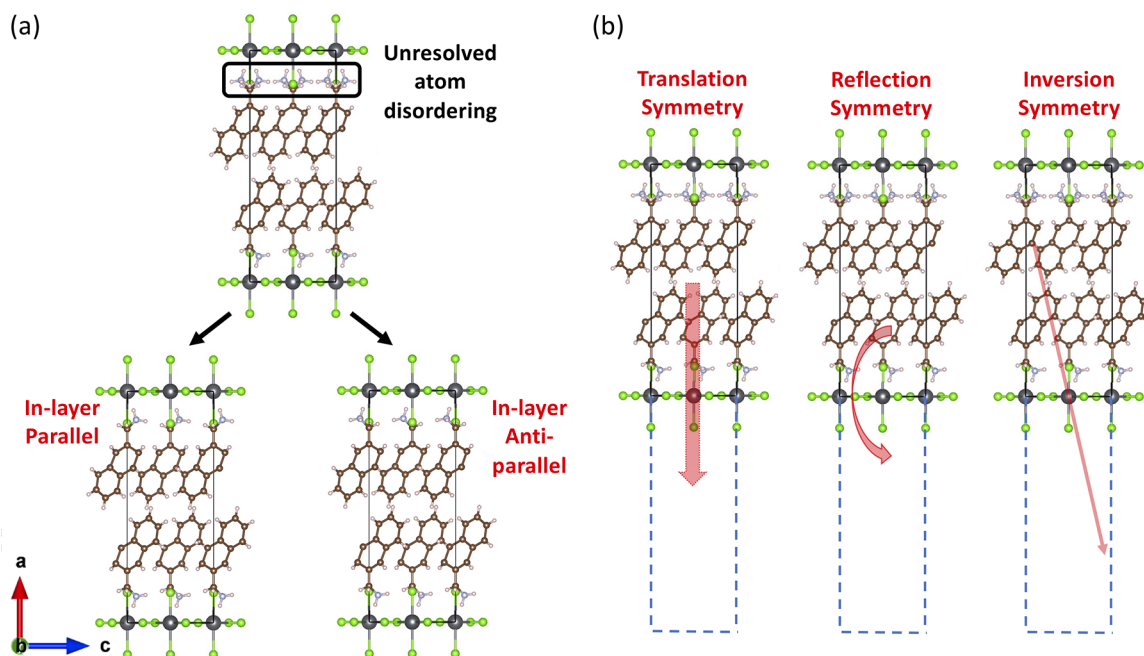


FIG. 3. Enumeration of five possible structures that are compatible with the  $(\text{NMA})_2\text{PbCl}_4$  single-layer unit cell. (a) Side view of one layer of the  $(\text{NMA})_2\text{PbCl}_4$  unit cell along the  $b$  axis after deleting overlapping atoms and unit cell alignment based on the ammonium groups in the lower part. With respect to the organic rings, only a parallel arrangement of the upper and lower layers is possible, whereas an antiparallel arrangement would lead to a steric conflict in the van der Waals gap. However, the upper row of ammonium groups can still be oriented either parallel or antiparallel with respect to their counterparts in the lower part, creating “in-layer parallel” (iP) and “in-layer antiparallel” (iA) conformations of the ammonium groups. (b) For a given single organic or inorganic layer [i.e., (a)], three different symmetry elements (translation, reflection, and inversion) can be used to construct the  $(\text{NMA})_2\text{PbCl}_4$  two-layer unit cell. By combining (a) and (b), six (i.e.,  $2 \times 3$ ) possible conformations result, of which two are equivalent, leading to a total of five distinct organic cation conformations that are compatible with the experimentally unresolved disorder in  $(\text{NMA})_2\text{PbCl}_4$ .

[Fig. 1(d)]. In addition to the present section, further details of the prototype structure construction are provided in a corresponding section at the beginning of the Supplemental Material [58].

An alternative pathway to find initial structure prototypes for a computational search of low-energy structures would be an exhaustive enumeration of all structure options within a predefined structure space of compounds. However, computationally exploring all structural degrees of freedom of the molecules and of the inorganic structure elements in structures as complex as those shown in Fig. 1 can easily lead to a combinatorial explosion of possibilities that becomes unmanageable even on current highest-performance computers. As one example, some of the authors recently explored a subspace of the structures of chiral adsorbate molecules on monolayer and bilayer perovskite platelets from first principles [77], leading to a combined search space of 8192 structures based on a still limited set of individual structure degrees of freedom. While future computational developments may alleviate this bottleneck, pursuing an exhaustive search was not an option for the present work. Likewise, the question of whether a newly predicted single-phase compound would even form or whether a more stable equilibrium of different solid-state or gas-phase secondary phases exists cannot be computationally answered, since a host of potential secondary phase equilibria is conceivable and not all possible secondary phases are even known. The experimentally known existence of at least six

of the 12 compounds studied here, however, indicates that the prospects for synthesizability of the other six are not unreasonable.

Generally, the inorganic lead halide octahedra in the 2D HOIPs structurally distort through Glazer tilting motions (see Fig. S1 in the Supplemental Material [58], Fig. 2 in Ref. [78], and Figs. S1–S3 in Ref. [59]), i.e., the in-plane Pb-X layers have an alternating arrangement of the “pinched-in” and “pinched-out” squares. For the 2D HOIPs studied here, all available experimental structures have lateral  $c(2 \times 2)$  unit cells and can accommodate this type of in-plane configuration. Figure 2 motivates the first eight structure options considered for each of the 12 compounds. The aligned unit cells of the five known compounds for which the experimental structure determinations resolve two inorganic or organic layers reveal three distinct degrees of freedom in the geometries of the organic moieties. In the case of the experimentally resolved structures, the particular geometry assumed in each case is already known, but in the experimentally unknown structures, these degrees of freedom, illustrated in Fig. 2, need to be resolved:

(i) *Tilting direction of the organic aromatic rings.* See Fig. 2(a), red vectors. When viewed along the  $b$  axis, the rings can be tilted either towards the  $+c$  direction [e.g.,  $(\text{PMA})_2\text{PbCl}_4$ ,  $(\text{PMA})_2\text{PbBr}_4$ ,  $(\text{PMA})_2\text{PbI}_4$ , and  $(\text{NMA})_2\text{PbBr}_4$ ] or towards the  $-c$  direction [e.g.,  $(\text{AMA})_2\text{PbCl}_4$ ]. This orientation difference is driven by the

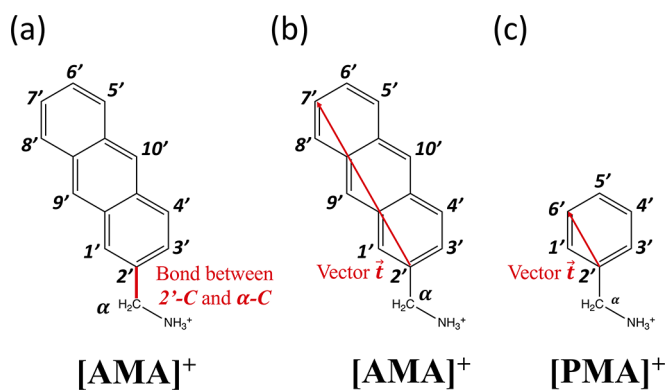


FIG. 4. For the  $\text{AMA}^+$  cation as an example, (a) the  $\sigma$  bond between the 2'-C atom and its corresponding  $\alpha$ -C atom and (b) the  $\vec{t}$  vector (from the 2'-C atom to the 7'-C atom) characterizing the tilting orientation of the oligoacene part. (c) The  $\text{PMA}^+$  cation contains only one benzene ring, leading to a different set of carbon indices. Thus the  $\vec{t}$  vector in  $\text{PMA}^+$  connects the 2'-C atom and the 6'-C atom.

rotation of the  $\sigma$  bond between the aromatic 2'-C atom and its corresponding  $\alpha$ -C atom [shown in Fig. 4(a)]. We use the connecting line between the 2'- and the 7'-C atoms of the aromatic rings to characterize the tilting orientation [red vectors  $\vec{t}$  in Figs. 4(b), 4(c), and 2(a)]. The angles between  $\vec{t}$  and all three crystallographic axes in the experimentally known structures are summarized in Table II. The orientation  $\vec{t}$  of other aromatic rings in each structure is then determined by each structure's translation and reflection symmetries.

(ii) *Symmetry element linking the upper and lower parts: mirror plane or inversion center.* See Fig. 2(b), atoms highlighted in red. Symmetry elements relating the structure above and below an inorganic plane can be either mirror planes [e.g., in  $(\text{PMA})_2\text{PbCl}_4$ ,  $(\text{PMA})_2\text{PbBr}_4$ ,  $(\text{NMA})_2\text{PbBr}_4$ , and  $(\text{AMA})_2\text{PbCl}_4$ ] or an inversion center [e.g., in  $(\text{PMA})_2\text{PbI}_4$ ].

(iii) *Packing pattern of two adjacent organic half layers.* See Fig. 2(c), red-dashed boxes. Adjacent half layers of organic cations can be packed either in a fashion in which vertical positions of their carbon atoms overlap (called “more densely packed” in the vertical direction or “more packed,” “MP” for short) or in a manner that avoids overlap of the coordinates of the organic rings projected on the  $a$  axis (called “less densely packed” in the vertical direction or “less packed,” “LP” for

TABLE II. Angles between the crystallographic axes  $a$ ,  $b$ , and  $c$  and the tilting vector  $\vec{t}$  of the organic rings (see text) in the experimentally known oligoacene methylammonium lead halide structures. Values are given in degrees. As noted in the text, the unresolved disorder present in the experimental  $(\text{NMA})_2\text{PbCl}_4$  XRD structure does not allow one to determine the tilting angle unambiguously.

System	$\vec{t}$ vs		
	$a$ axis	$b$ axis	$c$ axis
$(\text{PMA})_2\text{PbCl}_4$	36.24	72.85	59.25
$(\text{PMA})_2\text{PbBr}_4$	38.87	66.95	60.72
$(\text{PMA})_2\text{PbI}_4$	47.82	56.15	60.83
$(\text{NMA})_2\text{PbBr}_4$	37.31	76.44	56.08
$(\text{AMA})_2\text{PbCl}_4$	35.29	90.05	125.33

short). The MP pattern is associated with a distinctly lower separation distance between inorganic planes for the same organic cations. Details are provided in the beginning section of the Supplemental Material, which motivates that no clashes between atoms arise in the MP input structures (Figs. S1(a) and S2 [58]). As we will show below, using a MP pattern as a starting geometry for a structure optimization can lead to a LP final geometry. Thus, while we consider this packing feature as part of our structure search, there may not always be distinct local energy minima associated with MP or LP structures for the systems studied in this paper.

For all 12 compounds studied in this paper, we created  $2^3$  initial structures incorporating all combinations of features (i)–(iii) listed above. We identify structures as being “+c” or “-c” [feature (i)], having mirror plane (M) or inversion symmetry with an inversion center (I) [feature (ii)], and having less packed (LP) or more packed (MP) organic layers depending on the degree of overlap between the organic rings in adjacent organic half layers [feature (iii)]. This procedure defines the initial group of eight different geometries (mentioned above) to be considered for each compound and fully optimized using DFT-PBE+TS. We identify these input structures by simply concatenating the feature choices (i)–(iii) separated by slashes, e.g., “+c/M/LP.”

Figure 3 motivates the five further structure options considered for each of the 12 compounds. These five options enable us to fully accommodate the structural degrees of freedom left open by the superposition of organic cations in the experimental x-ray diffraction (XRD) structure of the  $(\text{NMA})_2\text{PbCl}_4$  compound [Fig. 1(d)]. The relative stacking order of adjacent inorganic planes in  $(\text{NMA})_2\text{PbCl}_4$  is different from the stacking order in the other five experimentally known compounds (see Fig. S1(b) [58]). In order to avoid unphysical overlapping hydrogen atoms in the van der Waals gap between the organic layers, adjacent organic rings in  $(\text{NMA})_2\text{PbCl}_4$  must be arranged parallel to one another, not antiparallel as for the other five known compounds [Figs. 1(a)–1(c), 1(e), and 1(f)].

Figure 3(a) shows that there are two possible ways in which the methylammonium tails at the top of an organic layer can be oriented with respect to the methylammonium tails at the bottom of an organic layer. This relative tail orientation is experimentally resolved in the five structures shown in Figs. 2(a)–2(c), 2(e), and 2(f) but not in the structure of  $(\text{NMA})_2\text{PbCl}_4$  [Fig. 2(d)]. Furthermore, the relative tail orientation is also unknown in the six experimentally unknown compounds and will therefore be considered as an additional degree of freedom. While Fig. 3(a) only shows a single organic layer, the structures considered in our structure searches include two organic layers each. As shown in Fig. 3(b), we therefore also need to consider the possible relative orientations of methylammonium tails that arise across two different organic layers, a total of three possibilities depending on whether the relation is defined by simple translation, reflection, or inversion operations. We denote the structure types derived from Fig. 3 as follows: (a) “in-layer parallel” or “in-layer antiparallel” ammonium tail orientation conformations (abbreviated as “iP” or “iA,” respectively) and (b) “Translation,” “Inversion,” or “Reflection.”

This means an input geometry will have the notation of, e.g., “iP+Translation” if the ammonium group orientation is



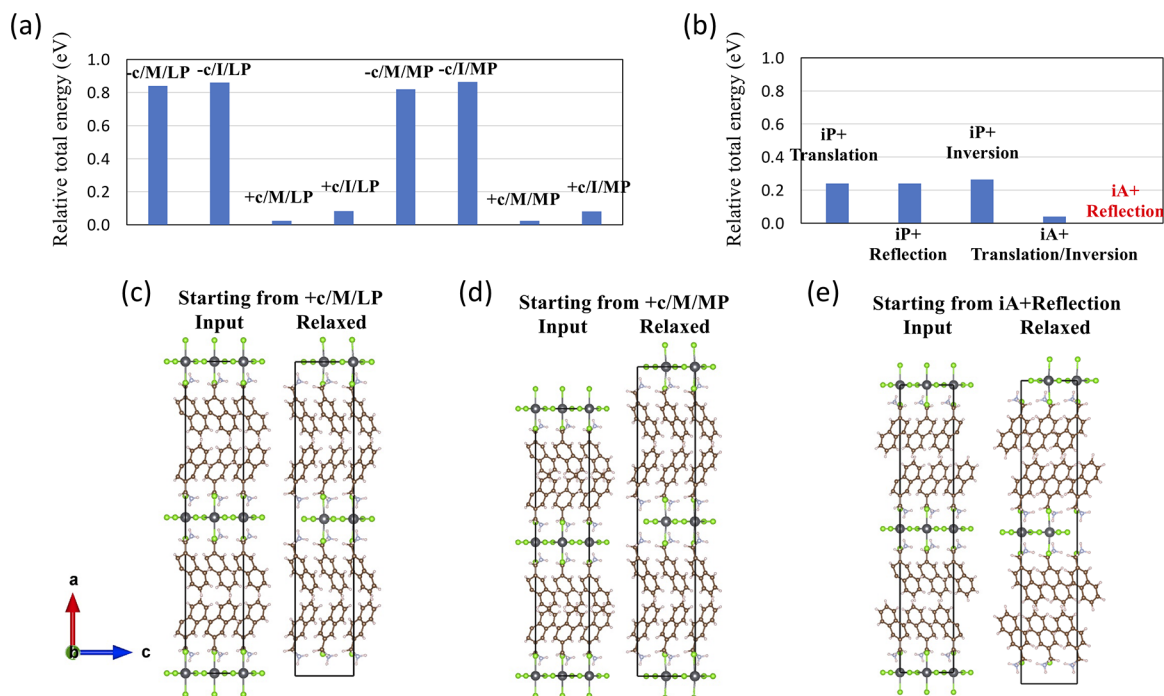


FIG. 5. Relative total energies and selected geometries associated with the DFT-PBE+TS geometry relaxation of  $(NMA)_2PbCl_4$ . (a) and (b) The relative total energies of the relaxed structures starting from the eight plus five initial geometries. The  $iA+$ Reflection relaxed structure leads to the lowest overall total energy, and total energies of other structures are reported relative to  $iA+$ Reflection. (c) The input and relaxed geometries of  $(NMA)_2PbCl_4$  starting from the  $+c/M/LP$  geometry. No significant geometry change is observed during the relaxation. (d) The input and relaxed geometries of  $(NMA)_2PbCl_4$  starting from the  $+c/M/MP$  geometry. The packed organic layers converge to the less packed configuration during the relaxation. (e) The input and relaxed geometries of  $(NMA)_2PbCl_4$  starting from the  $iA+$ Reflection geometry.

parallel inside each organic layer and if translational symmetry between the upper and lower organic layers is imposed. Together, Figs. 3(a) and 3(b) give rise to  $2 \times 3$ , i.e., six, apparent combinations. However, the  $iA+$ Translation and  $iA+$ Inversion structures turn out to be identical after symmetry analysis, leaving five inequivalent ways to relate the methylammonium tail orientations within each organic layer and across two organic layers.

### B. Total-energy calculations based on DFT-PBE+TS

As outlined in the previous section, we consider 13 distinct structure prototypes as possible configurations for each of the 12 organic-inorganic compounds studied in this paper. We begin by determining minimum-energy structures after full optimization of unit cell vectors and atomic positions by DFT-PBE+TS. In the five cases in which the experimental structure is known, the result of this total-energy comparison serves to validate our search approach. For the partially resolved  $(NMA)_2PbCl_4$  structure, we thus determine the lowest-energy and likely experimentally preferred organic cation arrangement, and finally, structure predictions are made for the experimentally unknown compounds.

For the example of  $(NMA)_2PbCl_4$ , Figs. 5(a) and 5(b) show the resulting total-energy comparison of the 13 possible input configurations after full energy minimization of all structural degrees of freedom. The reference energy is chosen to be the minimum-energy structure among them, which turns out to be the  $iA+$ Reflection arrangement, consistent with the

experimentally observed structure. Input and relaxed geometries of the overall lowest-energy conformation  $iA+$ Reflection are shown in Fig. 5(e). Indeed, none of the eight configurations included in Fig. 5(a) is compatible with the experimental arrangement [Fig. 1(d)], and all lead to higher energies than the  $iA+$ Reflection arrangement, even if only by a few tens of meV per unit cell in some cases. Figure 5(a) also shows that the energy difference is minimal between fully relaxed structures with less packed and more packed patterns as a starting point of otherwise analogous combinations of  $+c$  or  $-c$  and  $M$  or  $I$  after relaxation. As shown for the example of  $+c/M/LP$  and  $+c/M/MP$  in Figs. 5(c) and 5(d), the reason is that the two different starting configurations relax to the same final structure, which is the less packed structure in this case. We find the same behavior for other systems as well (see Supplemental Material, Tables S1–S4 and Figs. S3–S6 [58]).

Table III summarizes the most stable conformations for each compound considered in this paper as predicted by the DFT-PBE+TS relaxations. Geometry patterns are labeled with a superscript “a” if they are consistent with the experimentally known structure. Five out of six experimentally known structures are predicted in agreement with experiment. For  $(AMA)_2PbCl_4$ , the computational prediction ( $iA+$ Reflection) differs from the experimental observation ( $-c/M/LP$ ); that is, the ring arrangement between adjacent organic layers is predicted to be parallel, rather than antiparallel as is experimentally observed. The predicted  $iA+$ Reflection structure of  $(AMA)_2PbCl_4$  differs from the experimental structure mainly in the organic

TABLE III. The most stable conformations predicted by the DFT-PBE+TS relaxations. The first two columns are for the six experimentally known systems, and the third and fourth columns are for the six experimentally unknown systems.

Expt. known	Conformation	Expt. unknown	Conformation
(PMA) <sub>2</sub> PbCl <sub>4</sub>	+c/M/LP <sup>a</sup>	(NMA) <sub>2</sub> PbI <sub>4</sub>	+c/M/LP
(PMA) <sub>2</sub> PbBr <sub>4</sub>	+c/M/LP <sup>a</sup>	(AMA) <sub>2</sub> PbBr <sub>4</sub>	iA+Translation/Inversion
(PMA) <sub>2</sub> PbI <sub>4</sub>	+c/I/MP <sup>a</sup>	(AMA) <sub>2</sub> PbI <sub>4</sub>	iA+Translation/Inversion
(NMA) <sub>2</sub> PbCl <sub>4</sub>	iA+Reflection <sup>a</sup>	(TMA) <sub>2</sub> PbCl <sub>4</sub>	iA+Reflection
(NMA) <sub>2</sub> PbBr <sub>4</sub>	+c/M/LP <sup>a</sup>	(TMA) <sub>2</sub> PbBr <sub>4</sub>	iA+Translation/Inversion
(AMA) <sub>2</sub> PbCl <sub>4</sub>	iA+Reflection	(TMA) <sub>2</sub> PbI <sub>4</sub>	iA+Translation/Inversion

<sup>a</sup>Relaxed geometry patterns matching the experimentally obtained structures (if available).

moiety and has a similar set of lattice parameters. The energy difference per unit cell is rather large ( $-0.55$  eV). Since five out of six experimentally known structures are predicted correctly and one large outlier results, the previously reported experimental structure of (AMA)<sub>2</sub>PbCl<sub>4</sub> should be reevaluated (although this experimental reevaluation is outside the scope of this paper).

The lattice parameters of the optimized structures are summarized in Table IV, including a comparison with the experimental values if available. For (PMA)<sub>2</sub>PbCl<sub>4</sub>, (PMA)<sub>2</sub>PbBr<sub>4</sub>, (PMA)<sub>2</sub>PbI<sub>4</sub>, (NMA)<sub>2</sub>PbCl<sub>4</sub>, and (NMA)<sub>2</sub>PbBr<sub>4</sub>, the predicted geometric conformations and their relaxed lattice parameters closely match the experimental observation. The remaining discrepancy between predicted and measured lattice parameters does not exceed 2%, where the computed values consistently underestimate the experimental ones. One possible explanation for this underestimation is the neglect of any vibrational effects in the total-energy calculations, whereas the experimental structures include thermal expansion due to anharmonicities. Full details of all relaxed structures (lattice vectors and atomic coordinates) are provided as Tables S5–S16 [58] for reproducibility.

### C. Energy band alignments based on spin-orbit coupled DFT-HSE06

We next use the relaxed structures to study the impact of chemical composition on the band gap and charge carrier nature, i.e., quantum well character. Figures 6 and 7 show the DFT-HSE06+SOC band structures and frontier level alignments of all 12 systems. In Fig. 6, the Fermi level is set to the highest occupied state, and the overall gap is indicated for each system, using arrows to indicate the  $k$ -space location of the highest occupied and lowest unoccupied orbitals. In Fig. 7, a schematic plot of the frontier energy level alignments derived from organic and inorganic species, respectively, is shown. In this case, the energy axis is aligned with respect to the Pb 1s levels (the lowest-energy and therefore most localized core levels [59]). Frontier levels mainly contributed by the organic and inorganic components are represented by the red and blue lines in Fig. 7, and the corresponding organic and inorganic gaps are shown separately. Regarding the organic component, the extent of the  $\pi$ -conjugated systems increases from [PMA]<sup>+</sup> to [TMA]<sup>+</sup>, leading to a substantial predicted decrease of the energy difference between organic highest occupied and lowest unoccupied molecular orbitals ( $> 5$  eV for [PMA]<sup>+</sup>,  $\sim 4$  eV for [NMA]<sup>+</sup>,  $\sim 3.5$  eV for [AMA]<sup>+</sup>, and

$\sim 2.0$  eV for [TMA]<sup>+</sup>). Regarding the inorganic component, different halogen species also lead to a significant predicted decrease of the inorganic gap from  $\sim 3.4$  eV in Pb-Cl based systems to  $\sim 2.8$  eV in Pb-Br based systems and  $\sim 2.0$  eV in Pb-I based systems. The organic and inorganic frontier band levels are only slightly influenced by each other, suggesting that the frontier states from these two separate moieties are not hybridized [59]. It must be kept in mind that the actual band gap values in experimental specimens can deviate from the predicted band gaps by several tenths of an eV due to the unavoidable uncertainty of the density functional approximation used, but we expect the trends to hold.

Regarding their anticipated optical properties, the most interesting question is the relative alignment of the organic- and inorganic-derived frontier levels with respect to one another, in a quantum-well-like picture. Figure 7 shows that the energy levels of all systems studied here are predicted to be closest to a “type I” alignment, i.e., the highest occupied and lowest unoccupied energy levels are located on the same component. While we have not calculated dipole matrix elements, this trend nevertheless indicates that each of these systems is poised to absorb light strongly by band-edge-derived transitions. We can further separate the 12 compounds into those in which free carriers (holes and electrons) are expected to be localized on the inorganic vs on the organic component. In the language of Ref. [59], seven systems [all PMA and NMA based systems, as well as (AMA)<sub>2</sub>PbI<sub>4</sub>] are “type Ib” quantum wells, i.e., the band edges are formed by the inorganic component. This assignment is similar to many other layered HOIP materials with small and/or  $\sigma$ -bonded organic moieties, in which the organic band edges tend to be far apart. On the other hand, three systems show “type Ia” alignment, i.e., carriers are expected to be found on the organic moiety: (AMA)<sub>2</sub>PbCl<sub>4</sub>, (TMA)<sub>2</sub>PbCl<sub>4</sub>, and (TMA)<sub>2</sub>PbBr<sub>4</sub>, all of which have organic cations with a relatively small band gap and halide anions that correspond to relatively large gaps. Thus the quantum well alignment correlates with the sizes of the acene cations and of the halide anions, respectively: Smaller ions are associated with larger gaps in the respective organic or inorganic component. Combining a heavy halide anion (e.g., I<sup>−</sup>) with a smaller acene cation leads to clear type Ib alignment, whereas combining a light halide anion (e.g., Cl<sup>−</sup>) with a longer acene cation leads to clear type Ia alignment. It is interesting that two intermediate cases, (AMA)<sub>2</sub>PbBr<sub>4</sub> and (TMA)<sub>2</sub>PbI<sub>4</sub>, show essentially indistinguishable alignments of their organic- and inorganic-derived highest occupied and lowest unoccupied



TABLE IV. Comparison of the computationally predicted unit cell parameters of oligoacene methylammonium based HOIPs relaxed by DFT-PBE+TS. The experimental values are taken from Refs. [24–26,28,52].

Lattice parameter	$a$ (Å)	$b$ (Å)	$c$ (Å)	$\alpha$ (deg)	$\beta$ (deg)	$\gamma$ (deg)	$V$ (Å <sup>3</sup> )
(PMA) <sub>2</sub> PbCl <sub>4</sub>							
Expt.	33.62	7.82	7.73	90.0	90.0	90.0	2032
PBE+TS	33.36	7.75	7.60	90.0	90.0	90.0	1965
$\Delta$ (%)	-0.77	-0.90	-1.68	0.00	0.00	0.00	-3.32
(NMA) <sub>2</sub> PbCl <sub>4</sub>							
Expt.	41.72	7.75	7.79	90.0	90.0	90.0	2519
PBE+TS	41.58	7.74	7.62	90.0	90.0	90.0	2452
$\Delta$ (%)	-0.34	-0.13	-2.18	-0.01	-0.01	0.02	-2.64
(AMA) <sub>2</sub> PbCl <sub>4</sub>							
Expt.	50.44	7.52	7.73	90.0	90.0	90.0	2932
PBE+TS	49.61	7.61	7.58	90.0	90.0	91.1	2861
$\Delta$ (%)	-1.64	1.20	-1.94	-0.00	0.00	1.27	-2.42
(TMA) <sub>2</sub> PbCl <sub>4</sub>							
PBE+TS	57.06	7.57	7.60	90.0	90.0	90.0	3283
(PMA) <sub>2</sub> PbBr <sub>4</sub>							
Expt.	33.35	8.15	8.12	90.0	90.0	90.0	2207
PBE+TS	33.07	8.11	7.95	90.0	90.0	90.0	2132
$\Delta$ (%)	-0.84	-0.49	-2.09	0.00	0.04	0.00	-3.39
(NMA) <sub>2</sub> PbBr <sub>4</sub>							
Expt.	41.33	8.08	8.08	90.0	90.0	90.0	2698
PBE+TS	40.85	8.02	8.03	90.0	90.0	90.0	2631
$\Delta$ (%)	-1.16	-0.74	-0.62	0.00	0.00	0.01	-2.50
(AMA) <sub>2</sub> PbBr <sub>4</sub> <sup>a</sup>							
PBE+TS	47.83	7.90	8.05	90.0	89.1	90.0	3041
(TMA) <sub>2</sub> PbBr <sub>4</sub>							
PBE+TS	54.68	7.83	8.07	90.0	90.1	90.0	3455
(PMA) <sub>2</sub> PbI <sub>4</sub>							
Expt.	28.78	9.16	8.69	90.0	90.0	90.0	2291
PBE+TS	28.52	9.19	8.54	90.0	90.0	90.0	2238
$\Delta$ (%)	-0.90	0.33	-1.73	-0.02	0.01	0.02	-2.29
(NMA) <sub>2</sub> PbI <sub>4</sub>							
PBE+TS	39.75	8.51	8.53	90.0	90.0	90.0	2885
(AMA) <sub>2</sub> PbI <sub>4</sub> <sup>a</sup>							
PBE+TS	46.29	8.42	8.57	90.0	88.6	90.0	3369
(TMA) <sub>2</sub> PbI <sub>4</sub>							
PBE+TS	52.45	8.38	8.51	90.0	89.0	90.0	3740

<sup>a</sup>The structural parameters given here for (AMA)<sub>2</sub>PbBr<sub>4</sub> and (AMA)<sub>2</sub>PbI<sub>4</sub> differ from those obtained in the actual relaxation (shown in Fig. S5 and Tables S12 and S13 [58]), since two lattice vectors can be combined to yield a  $\beta$  angle close to 90°, as well as a shorter lattice vector (close to the interplanar distance), in line with the convention used for other compounds. The band structure calculations shown in Fig. 6 were carried out using the relaxed geometries given in Tables S12 and S13 [58].

levels. Specifically, the difference between inorganic and organic lowest unoccupied states is  $\sim 1$  meV in (AMA)<sub>2</sub>PbBr<sub>4</sub> and is  $\sim 4$  meV in (TMA)<sub>2</sub>PbI<sub>4</sub>, indicating that free carriers should be able to flow without much inhibition between either component. These two systems are therefore interesting candidates for further, more detailed studies of their absorption, emission, and/or transport properties. For example, diffusion of excitons is a possibility in these systems, depending on the magnitude of exciton binding energies and other effects, such as polaronic contributions, which are not considered here. Notably, our DFT-HSE06+SOC based analysis does not address detailed excitonic effects such as the formation and energies of singlet vs triplet levels in the organic subsystems. For example, Ref. [40] shows that energy can transfer between

the lead chloride exciton band and the naphthyl triplet system of (NMA)<sub>2</sub>PbCl<sub>4</sub>. Qualitatively, this observation is consistent with our predicted band alignment (without excitonic effects) if the triplet exciton binding energy on the naphthyl system is substantially larger than the binding energy associated with excitons derived from the lead chloride bands.

Given the potential interest in the singlet fission properties of acene-derived materials in the context of PV, a few further comments are in order. First, and importantly, for singlet fission to be effective, the energy of triplet excitons must be around a factor of 2 lower than the energy of singlet excitons. For instance, past experimental estimates in tetracene single crystals and pentacene thin films place their triplet exciton energies at 1.25 and 0.86 eV, respectively [79]. As bulk solids of tetracene and pentacene are not necessarily indicative of

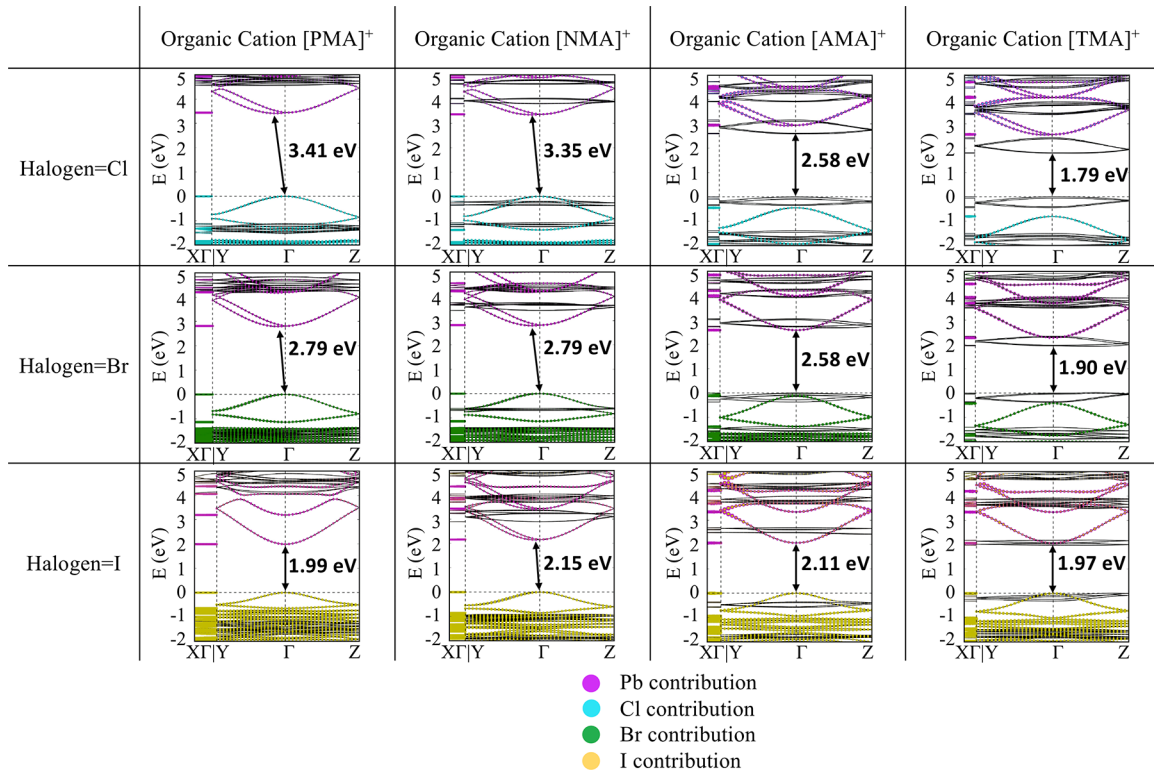


FIG. 6. DFT-HSE06+SOC band structures based on the most stable relaxed geometries of each compound studied in this paper. Bands on the three featured  $k$ -path segments ( $\Gamma$ -X, Y- $\Gamma$ , and  $\Gamma$ -Z; see Supplemental Material, Fig. S8 [58], for an image of the Brillouin zone orientation in relation to the real-space unit cells) and band gap values are shown in each plot. Highest occupied and lowest unoccupied states are indicated by arrows. Bands with dominant inorganic-derived contributions are highlighted by purple, cyan, green, and yellow dots for majority contributions from Pb, Cl, Br, and I, respectively. Black lines indicate organic-derived bands. The energy scale ( $y$  axis) is aligned to the valence band maximum as the zero value for each compound.

acene layers of the 2D perovskite materials studied here, it is unlikely that singlet fission in tetracene or pentacene layers can be directly exploited by charge separating triplet excitons into separate carriers and transferring them back to the 2D inorganic moieties, which have much higher fundamental gaps. Indeed, the singlet fission prospects of tetracene or pentacene are typically studied in conjunction with much-lower-band-gap semiconductors, such as Si [80,81]. Three-dimensional perovskites have lower band gaps than their 2D analogs, offering potentially better charge extraction opportunities, but a previous study involving tetracene in contact with 3D perovskites did not result in observable triplet transfer [27]. This observation is consistent with either an energetic uphill step in the actual singlet fission of tetracene [79] or an uphill step in the transfer to the 3D perovskite. However, other routes to exploit the templating of anchored acene layers afforded by 2D inorganic perovskites could still be imagined, e.g., by using the inorganic moiety to enhance absorption in close proximity to a well-ordered acene film. The close band alignments of some of the materials investigated in Figs. 6 and 7 suggest that singlet excitons generated on the strongly absorbing inorganic component of very thin 2D hybrid perovskite films could have the ability to transfer to the singlet states of well-ordered, perovskite-templated tetracene or (not investigated in this paper) pentacene layers. These singlet excitons may then be amenable to conversion to two triplet excitons within the or-

ganic component and could be extractable as separate charges at interfaces with connected lower-gap semiconductors.

In Table V, we provide a comparison of our predicted fundamental band gap values with literature values of both experimentally determined absorption gaps and computed quasiparticle and excitonic gaps from the high-level  $GW$  and  $GW+BSE$  approaches [75]. As discussed in more detail in Sec. II, we expect that the absolute, calculated DFT-HSE06+SOC fundamental gap values can be underestimated by several tenths of an eV for lead halide based 2D HOIPs. Table V shows that the experimental *absorption* gaps uniformly reside above the DFT-HSE06+SOC *fundamental* gap values by 0.3–0.4 eV. Typical exciton binding energies are of the order of  $\sim 0.3$  eV or higher; that is, a systematic underestimation of fundamental gaps by  $\sim 0.6$  eV (similar to phenethylammonium lead iodide) is plausible and also borne out by the  $GW$  and  $GW+BSE$  literature values. As also outlined in Sec. II, our past experience suggests that the qualitative quantum well type predictions in Fig. 7 are more reliable, attributed to compensation of systematic errors. Likewise, the predicted intraband topology [i.e., spin splitting observed in inorganic-derived conduction bands (CBs), discussed in the next section], which is dictated by symmetry, is not expected to be affected as much by details of the density functional method as the absolute value of the predicted fundamental gap.

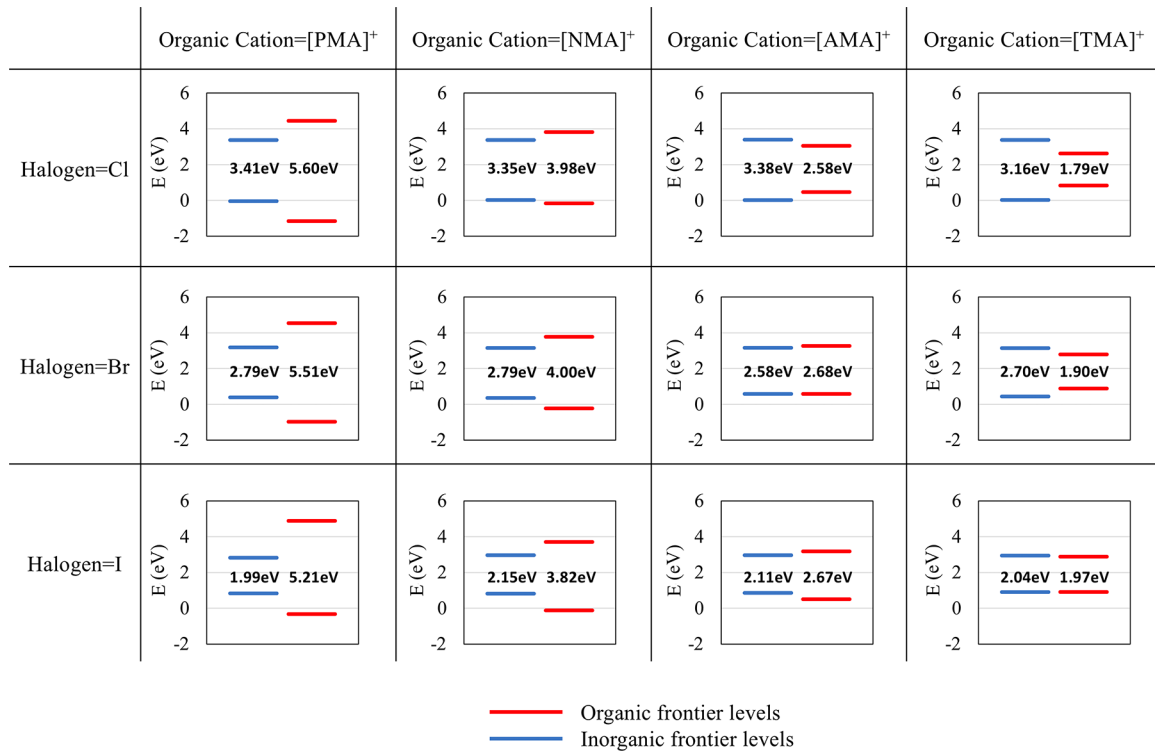


FIG. 7. Summary of the frontier energy level alignments based on the DFT-HSE06+SOC electronic structure calculations in Fig. 6. In contrast to Fig. 6, the energy axes ( $y$  axes) of all 12 systems are aligned such that their Pb  $1s$  states (lowest-lying core states, not shown in the figure) have equal energy values. Red and blue lines represent the frontier levels contributed by the organic and inorganic components, respectively.

#### D. Frontier orbital character and inversion-asymmetry-induced spin splitting based on spin-orbit coupled DFT-HSE06

The final part of our analysis focuses on the character of the frontier bands, particularly with an eye towards local vs global inversion asymmetry and the potential for spin splitting in the conduction bands. In the band structure plots (Fig. 6), the  $\Gamma$ - $X$  direction in the reciprocal space corresponds to the stacking direction of inorganic 2D planes while the  $Y$ - $\Gamma$  and  $\Gamma$ - $Z$  directions correspond to the two “in-plane” directions of 2D HOIPs (Fig. S8). Due to the spatial separation along the stacking direction in the real space, inorganic-derived bands are practically flat along  $\Gamma$ - $X$ , consistent with a lack of orbital overlap between adjacent inorganic layers and/or

adjacent organic layers, respectively. Additionally, as shown by the arrows in Fig. 6, the inorganic highest occupied and lowest unoccupied states of  $(\text{PMA})_2\text{PbCl}_4$ ,  $(\text{PMA})_2\text{PbBr}_4$ ,  $(\text{NMA})_2\text{PbCl}_4$ ,  $(\text{NMA})_2\text{PbBr}_4$ , and  $(\text{NMA})_2\text{PbI}_4$ , i.e., their inorganic-derived valence band maxima and conduction band minima, form momentum-forbidden indirect band gaps near the  $\Gamma$  point. This feature is an outcome of the relativistic spin splitting effects that are apparent in the inorganic conduction bands. Specifically, SOC together with the breaking of inversion symmetry in the crystal leads to a splitting of what would be a nominally degenerate conduction band (with local inversion symmetry in the inorganic plane) into separate bands with distinct spin expectation values at given  $k$  points and with

TABLE V. Comparison of previously reported band gap data of the six experimentally known oligoacene based 2D HOIP systems with DFT-HSE06+SOC predicted fundamental gaps in this paper, including whether the calculated gap is derived from the inorganic (i) or the organic (o) component. The experimental data reflect room-temperature (298 K) and low-temperature (1.5 K) absorption onset energies  $E_{\text{abs,expt}}$ , which (unlike our DFT-HSE06+SOC predictions) include excitonic effects. The calculated values  $E_{g,\text{theor}}$  also include  $GW$  @(PBE+SOC) quasiparticle band gaps and  $(GW+BSE)$  @(PBE+SOC) gaps (the latter including the predicted exciton binding energy).

	$E_{\text{abs,expt}}$ (eV)		$E_{g,\text{theor}}$ (eV)		
	298 K	1.5 K	$GW$ @(PBE+SOC)	$(GW+BSE)$ @(PBE+SOC)	HSE06+SOC (this paper)
$(\text{PMA})_2\text{PbCl}_4$	3.72 [26]				3.41 (i)
$(\text{PMA})_2\text{PbBr}_4$	3.11 [26]		2.95 [75]	2.48 [75]	2.79 (i)
$(\text{PMA})_2\text{PbI}_4$	2.41 [26]	–			1.99 (i)
$(\text{NMA})_2\text{PbCl}_4$	3.74 [26]	3.61 [40]			3.35 (i)
$(\text{NMA})_2\text{PbBr}_4$	3.16 [26]		3.10 [75]	2.65 [75]	2.79 (i)
$(\text{AMA})_2\text{PbCl}_4$		2.97 [40]			2.58 (o)



off- $\Gamma$  locations of the actual conduction band minima [82]. Due to their heavier nuclei, Pb-6*p*-derived states experience much stronger SOC effects than *p* states derived from the halogen atoms Cl (3*p* valence states), Br (4*p* valence states), and I (5*p* valence states). Therefore the inorganic conduction bands (which are derived from the Pb 6*p* states) show stronger SOC effects than the inorganic valence bands.

As is apparent from Fig. 6, five PMA- and NMA-containing systems, (PMA)<sub>2</sub>PbCl<sub>4</sub>, (PMA)<sub>2</sub>PbBr<sub>4</sub>, (NMA)<sub>2</sub>PbCl<sub>4</sub>, (NMA)<sub>2</sub>PbBr<sub>4</sub>, and (NMA)<sub>2</sub>PbI<sub>4</sub>, show off- $\Gamma$  conduction band minima. Three of them [(PMA)<sub>2</sub>PbCl<sub>4</sub>, (PMA)<sub>2</sub>PbBr<sub>4</sub>, and (NMA)<sub>2</sub>PbBr<sub>4</sub>] indeed adopt inversion-asymmetric structures in experiment (see Table I). One of them [(NMA)<sub>2</sub>PbCl<sub>4</sub>] does adopt an inversion-symmetric experimental structure, but this is the special case in which experimental data did not resolve the structure fully. Our predicted, fully resolved version of this structure (iA+Reflection in Fig. 5) is globally inversion asymmetric, qualitatively in line with its neighbors (PMA)<sub>2</sub>PbCl<sub>4</sub>, (PMA)<sub>2</sub>PbBr<sub>4</sub>, and (NMA)<sub>2</sub>PbBr<sub>4</sub>. Finally, the experimentally unknown compound (NMA)<sub>2</sub>PbI<sub>4</sub> is also predicted to be inversion asymmetric in this paper, as demonstrated by a more detailed analysis of Pb-I-Pb bond angles further below. The compound (PMA)<sub>2</sub>PbI<sub>4</sub> is inversion symmetric in experiment, and that is confirmed by our predictions as well. Consistently, no spin splitting is seen in its conduction bands, and its predicted band gap is direct at the  $\Gamma$  point. In Fig. S9, we show computed spin textures of the frontier energy bands of the six PMA- and NMA-derived compounds, which demonstrate that the split bands of the five inversion-asymmetric compounds indeed have opposite expectation values of their out-of-plane spin components ( $\langle\sigma_x\rangle$ ), as one would expect.

Regarding the six AMA- and TMA-derived compounds, only (AMA)<sub>2</sub>PbCl<sub>4</sub> has an experimentally determined counterpart so far. Its experimental structure is inversion asymmetric. As noted in Table III, however, our predicted structure for this compound favors another conformation, iA+Reflection, by a substantial total-energy amount (−0.55 eV per unit cell; see above). This structure is also inversion asymmetric, and correspondingly, the inorganic-derived conduction bands show a spin-splitting-like structure in Fig. 6. For completeness, Fig. S7 shows the band structure and band alignment of its experimentally claimed structure as well, revealing qualitatively similar characteristics to the band structure and alignment and inorganic conduction band spin splitting of the predicted structure. For the experimentally unknown Cl-derived compound, (TMA)<sub>2</sub>PbCl<sub>4</sub>, we also predict an inversion-asymmetric structure (i.e., all Cl-derived compounds studied in this paper spontaneously break inversion symmetry), and a corresponding spin splitting is seen in its inorganic conduction bands. Interestingly, the four Br- and I-derived (experimentally unknown) AMA- and TMA-derived compounds are all predicted to adopt inversion-symmetric structures and therefore do not show any spin splitting features in their inorganic conduction bands.

In a previous study [51], some of us demonstrated that spin splitting in layered perovskites due to inversion symmetry breaking can be qualitatively predicted by a “structural descriptor,” specifically, a difference between the in-plane

TABLE VI. Summary of the in-plane Pb-X-Pb ( $X = \text{Cl, Br, I}$ ) bond angle disparity (taken from the computationally relaxed structures) and the spin splitting magnitude ( $\Delta E_{\pm}$ ) of the lowest inorganic conduction bands in different 2D HOIP systems.

Compound	Pb-X-Pb disparity (deg)	$\Delta E_{\pm}$ (meV)
(PMA) <sub>2</sub> PbCl <sub>4</sub>	14.6	123.2
(PMA) <sub>2</sub> PbBr <sub>4</sub>	11.7	79.8
(NMA) <sub>2</sub> PbCl <sub>4</sub>	12.5	71.7
(NMA) <sub>2</sub> PbBr <sub>4</sub>	12.0	81.1
(NMA) <sub>2</sub> PbI <sub>4</sub>	7.3	29.1
(AMA) <sub>2</sub> PbCl <sub>4</sub>	12.1	64.9
(TMA) <sub>2</sub> PbCl <sub>4</sub>	11.0	61.8

Pb-X-Pb bond angles ( $\alpha, \delta$ ) and ( $\beta, \gamma$ ), which are defined in Fig. 8(a) and which can be quantified in all unit cells investigated in this paper. Figure 8(a) depicts the central inorganic layer of the computationally relaxed (PMA)<sub>2</sub>PbCl<sub>4</sub> structure as an example. In this case,  $\alpha = \delta = 151.8^{\circ}$  and  $\beta = \gamma = 137.2^{\circ}$ . This predicted noncentrosymmetric distortion pattern also exists in the experimental structure, in which  $\alpha = \delta = 154.9^{\circ}$  and  $\beta = \gamma = 142.0^{\circ}$ . This bond angle difference between the ( $\alpha, \delta$ ) and ( $\beta, \gamma$ ) of  $\sim 13^{\circ}$ – $15^{\circ}$  is among the largest of such differences tabulated in Ref. [51] for several known chiral structures (i.e., layered perovskites that include a chiral organic cation). As shown in Fig. 8(b), the  $\alpha$ -C-NH<sub>3</sub><sup>+</sup> groups above and below the middle inorganic layer point towards the same direction in (PMA)<sub>2</sub>PbCl<sub>4</sub>, but they point towards the reverse direction in the inversion-symmetric counterpart (PMA)<sub>2</sub>PbI<sub>4</sub>, leading to heterogeneous and homogeneous chemical environments for different in-plane halide atoms, respectively. Thus the in-plane Cl atoms in (PMA)<sub>2</sub>PbCl<sub>4</sub> have two sets of different chemical environments, which determine the in-plane angle disparity and the associated spin splitting. More details of the chemical environment analysis are shown in the Supplemental Material, Figs. S10 and S11 [58].

Table VI summarizes the in-plane Pb-X-Pb ( $X = \text{Cl, Br, I}$ ) bond angle disparity values (in the predicted stable structures) and the spin splitting magnitude in the 2D HOIPs (PMA)<sub>2</sub>PbCl<sub>4</sub>, (PMA)<sub>2</sub>PbBr<sub>4</sub>, (NMA)<sub>2</sub>PbCl<sub>4</sub>, (NMA)<sub>2</sub>PbBr<sub>4</sub>, (NMA)<sub>2</sub>PbI<sub>4</sub>, (AMA)<sub>2</sub>PbCl<sub>4</sub>, and (TMA)<sub>2</sub>PbCl<sub>4</sub>, where spin splitting exists in the lowest inorganic conduction band (shown in Fig. 6). For simplicity, we use the energy difference between the spin-reverse band branches at the inorganic conduction band minimum ( $\Delta E_{\pm}$ ) to quantify the magnitude of the inorganic-derived spin splitting. We find that these seven data points match the corresponding structure-property relationship reported in Ref. [51] very well, supporting the nominally linear numerical relationship between the in-plane bond angle disparity and inorganic spin splitting.

As shown in Fig. 8(c) and Table VI, similar and large Pb-Cl-Pb bond angle disparities are present for all Cl based acene-containing layered perovskites studied here; that is, the observed asymmetry of the inorganic layer is predicted to be universal among the Pb-Cl and methylammonium acene cation based layered perovskites. Among the Br based

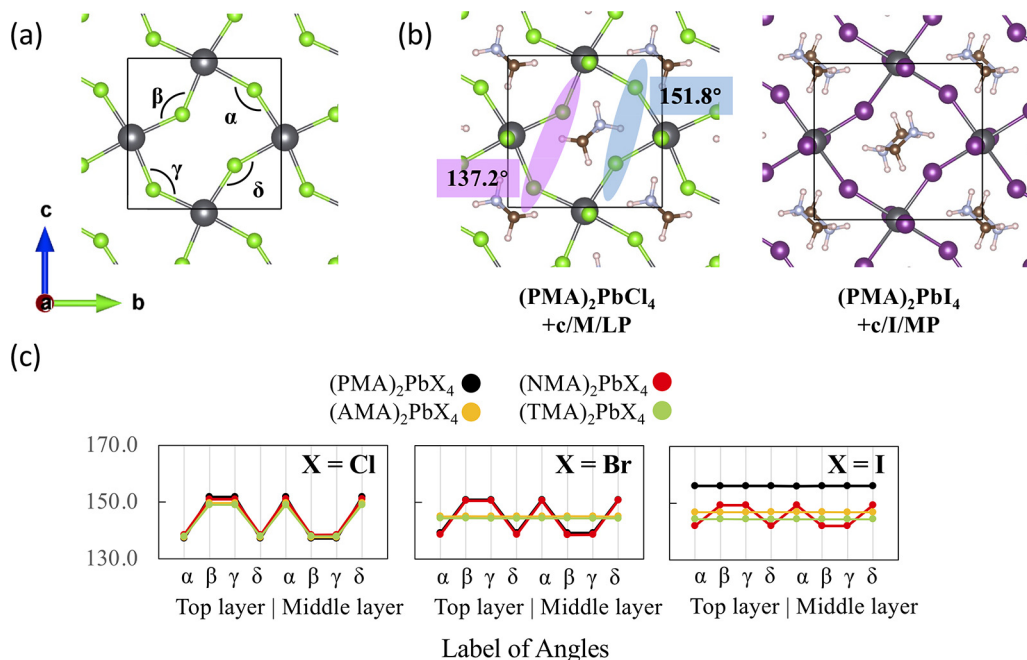


FIG. 8. A summary of the in-plane bond angle disparity analysis. (a) Taking the middle inorganic layer of  $(\text{PMA})_2\text{PbCl}_4$  as an example, the labels of the in-plane bond angles used in this analysis are shown. (b) Taking the  $(\text{PMA})_2\text{PbCl}_4$  and  $(\text{PMA})_2\text{PbI}_4$  as examples, the orientations of the  $\alpha\text{-C-NH}_3^+$  groups right above and below the middle inorganic layer are presented. Different from  $(\text{PMA})_2\text{PbI}_4$ , the reflection symmetry between the upper and lower organic layers in  $(\text{PMA})_2\text{PbCl}_4$  creates two different chemical environments for the in-plane Cl atoms, which is highlighted in blue and purple. (c) A plot showing the in-plane bond angle disparity of all 12 systems in this paper. The in-plane Pb-X-Pb ( $X = \text{Cl, Br, I}$ ) bond angles of  $(\text{PMA})_2\text{PbCl}_4$ ,  $(\text{PMA})_2\text{PbBr}_4$ ,  $(\text{NMA})_2\text{PbCl}_4$ ,  $(\text{NMA})_2\text{PbBr}_4$ ,  $(\text{NMA})_2\text{PbI}_4$ ,  $(\text{AMA})_2\text{PbCl}_4$ , and  $(\text{TMA})_2\text{PbCl}_4$  show significant noncentrosymmetric disparities. This feature matches the observed spin splitting in inorganic CBs in Fig. 6.

variants, only the smaller acene cations PMA and NMA allow for a similarly large bond angle distortion, whereas the layered Pb-Br perovskites with larger acenes, AMA and TMA, revert to inversion-symmetric configurations as discussed above. Finally, for Pb-I based methylammonium acene perovskites, only the NMA based variant is predicted to exhibit a significant bond angle asymmetry and thus spin splitting in its inorganic-derived bands. Although smaller than in the Br and Cl based cases, the bond angle disparity in  $(\text{NMA})_2\text{PbI}_4$  is still sizable (see Table VI). It would be interesting to determine if associated spintronic and chiroptical phenomena can be experimentally accessed in the nominally (as per its individual components) achiral, iodide based layered perovskite  $(\text{NMA})_2\text{PbI}_4$ .

#### IV. CONCLUSION

This work computationally assesses the structural and electronic properties of methylammonium acene based lead halide layered hybrid perovskites. The study covers 12 compounds (Table I), including  $\text{Cl}^-$ ,  $\text{Br}^-$ , and  $\text{I}^-$  as halide anions and phenylmethylammonium (one ring) through tetrylmethylammonium (four rings) as organic cations. The major findings are structure predictions (including known and hitherto unsynthesized compounds), band gap tunability, important for possible electronic and optoelectronic applications, and relativistic spin splitting of the frontier energy bands as a consequence of spontaneous inversion symmetry breaking, important for potential chiroptical and spintronic applications.

Regarding structural properties, our assessment of possible organic-inorganic configurations coincides with the experimentally reported XRD structures of four acene based HOIPs, i.e.,  $(\text{PMA})_2\text{PbCl}_4$ ,  $(\text{PMA})_2\text{PbBr}_4$ ,  $(\text{PMA})_2\text{PbI}_4$ , and  $(\text{NMA})_2\text{PbBr}_4$ . For  $(\text{NMA})_2\text{PbCl}_4$ , we resolve the residual disorder (superimposed molecules) of the organic layer present in the past experimental structure refinement. For  $(\text{AMA})_2\text{PbCl}_4$ , our predicted lowest-energy configuration deviates from the experimental structure, with an energy difference per unit cell of  $\sim 0.55$  eV. This difference is large in view of systematic errors of the theory and suggests that the experimental structure of  $(\text{AMA})_2\text{PbCl}_4$  should be revisited.

Regarding electronic properties, the band gap is tunable. All materials are predicted to be type I quantum wells, i.e., the frontier orbitals are located on the same component (organic or inorganic). In seven compounds, the frontier orbitals are unambiguously predicted to be localized on the inorganic component, with a predicted accessible band gap between 2.11 eV [ $(\text{NMA})_2\text{PbI}_4$ ] and 3.41 eV [ $(\text{PMA})_2\text{PbCl}_4$ ]. In three compounds, the frontier orbitals are unambiguously localized on the organic component, with predicted band gaps ranging from 1.79 eV [ $(\text{TMA})_2\text{PbCl}_4$ ] through 2.58 eV [ $(\text{AMA})_2\text{PbCl}_4$ ]. As discussed in more detail in the appropriate sections, these predicted fundamental gap values underestimate the experimentally known absorption onsets by  $\sim 0.3\text{--}0.4$  eV, and the underestimation of experimental fundamental gap values is expected to be even larger. Nevertheless, in view of photovoltaic applicability (e.g., singlet-fission-type approaches), the lowest predicted

gap among the 12 systems considered here,  $E_g = 1.79$  eV for  $(\text{TMA})_2\text{PbCl}_4$ , may still be in a relevant range, especially if further excitonic and/or vibronic corrections [74] to the expected optical response are considered. As noted in our discussion, it is unlikely that singlet-triplet conversion would be effectively exploitable in a thick 2D perovskite film, but a more sophisticated interface of an ultrathin 2D hybrid, acene based perovskite film could potentially allow one to take advantage of triplet generation. Finally, substantial relativistic spin splitting occurs in the inorganic-derived conduction bands of  $(\text{PMA})_2\text{PbCl}_4$ ,  $(\text{PMA})_2\text{PbBr}_4$ ,  $(\text{NMA})_2\text{PbCl}_4$ ,  $(\text{NMA})_2\text{PbBr}_4$ , and  $(\text{NMA})_2\text{PbI}_4$ , due to spontaneous breaking of inversion symmetry. These results raise the exciting possibility of realizing spintronic and/or chiroptical properties with deliberately tunable band gaps and other electronic and optoelectronic properties in future devices composed of single-crystalline versions of the above materials,

As noted in the Introduction, the synthesis of HOIPs based on large conjugated oligoacene molecules such as anthracene or tetracene presents additional experimental challenges due to the low solubility of these molecules in solvents that also dissolve lead halides. The recent demonstration of resonant infrared matrix-assisted pulsed laser evaporation (RIR-MAPLE) enabling the fabrication of 2D HOIPs based on large conjugated oligothiophene molecules [60] as well as of halide alloyed phenethylammonium lead HOIPs [64] may assist in future syntheses of layered HOIPs containing multiring acenes. Similarly, targeted functionalizations may

enhance synthesizability, as also demonstrated in the oligothiophene space [63].

The most stable geometries (predicted by DFT-PBE+TS) of all 12 compounds discussed in this paper and their corresponding band structures were deposited into the Hybrid<sup>3</sup> database. They can be accessed [83]. The FHI-AIMS input and output files associated with this study were deposited in the NOMAD database and can be accessed [84]. The 156 “geometry.in” input files used as starting points to identify lowest-energy structures are publicly available [85].

## ACKNOWLEDGMENTS

This work was primarily funded by the National Science Foundation (NSF) DMREF program under Awards No. DMR-1729297 and No. DMR-1728921. C.L. was financially supported by the NSF under Awards No. DMR-1729297 and No. DMR-1728921, as well as through the Research Triangle MRSEC (NSF Award No. DMR-11-21107). We would like to thank the University of North Carolina at Chapel Hill and the Research Computing group for providing computational resources and support. Computer time was also provided by the National Energy Research Scientific Computing Center (NERSC), a U.S. Department of Energy (DOE) Office of Science User Facility operated under Contract No. DEAC02-05CH11231.

- 
- [1] A decade of perovskite photovoltaics, *Nat. Energy* **4**, 1 (2019).
- [2] L. Mar, Perovskite fever, *Nat. Mater.* **13**, 837 (2014).
- [3] M. D. McGehee, Continuing to soar, *Nat. Mater.* **13**, 845 (2014).
- [4] National Renewable Energy Laboratory, NREL Best Research-Cell Efficiency Chart, retrieved October 21, 2022, <https://www.nrel.gov/pv/assets/pdfs/best-research-cell-efficiencies-rev220630.pdf>.
- [5] D. B. Mitzi, K. Chondroudis, and C. R. Kagan, Organic-inorganic electronics, *IBM J. Res. Dev.* **45**, 29 (2001).
- [6] B. R. Sutherland and E. H. Sargent, Perovskite photonic sources, *Nat. Photonics* **10**, 295 (2016).
- [7] Q. Zhang, R. Su, W. Du, X. Liu, L. Zhao, S. T. Ha, and Q. Xiong, Advances in small perovskite-based lasers, *Small Methods* **1**, 1700163 (2017).
- [8] H. Dong, C. Zhang, X. Liu, J. Yao, and Y. S. Zhao, Materials chemistry and engineering in metal halide perovskite lasers, *Chem. Soc. Rev.* **49**, 951 (2020).
- [9] K. Lin, J. Xing, L. N. Quan, F. De Arquer, X. Gong, J. Lu, L. Xie, W. Zhao, D. Zhang, C. Yan, W. Li, X. Liu, Y. Lu, J. Kirman, E. H. Sargent, Q. Xiong, and Z. Wei, Perovskite light-emitting diodes with external quantum efficiency exceeding 20 per cent, *Nature (London)* **562**, 245 (2018).
- [10] W. Tian, H. Zhou, and L. Li, Hybrid organic-inorganic perovskite photodetectors, *Small* **13**, 1702107 (2017).
- [11] P. Kanhere and Z. Chen, A review on visible light active perovskite-based photocatalysts, *Molecules* **19**, 19995 (2014).
- [12] G. Zhang, G. Liu, L. Wang, and J. T. Irvine, Inorganic perovskite photocatalysts for solar energy utilization, *Chem. Soc. Rev.* **45**, 5951 (2016).
- [13] G. Long, R. Sabatini, M. I. Saidaminov, G. Lakhwani, A. Rasmita, X. Liu, E. H. Sargent, and W. Gao, Chiral-perovskite optoelectronics, *Nat. Rev. Mater.* **5**, 423 (2020).
- [14] A. Privitera, M. Righetto, F. Cacialli, and M. K. Riede, Perspectives of organic and perovskite-based spintronics, *Adv. Opt. Mater.* **9**, 2100215 (2021).
- [15] Y.-H. Kim, Y. Zhai, H. Lu, X. Pan, C. Xiao, E. A. Gaulding, S. P. Harvey, J. J. Berry, Z. V. Vardeny, J. M. Luther, and M. C. Beard, Chiral-induced spin selectivity enables a room-temperature spin light-emitting diode, *Science* **371**, 1129 (2021).
- [16] H. Lu, C. Xiao, R. Song, T. Li, A. E. Maughan, A. Levin, R. Brunecky, J. J. Berry, D. B. Mitzi, V. Blum, and M. C. Beard, Highly distorted chiral two-dimensional tin iodide perovskites for spin polarized charge transport, *J. Am. Chem. Soc.* **142**, 13030 (2020).
- [17] Y.-H. Kim, R. Song, J. Hao, Y. Zhai, L. Yan, T. Moot, A. F. Palmstrom, R. Brunecky, W. You, J. J. Berry, J. L. Blackburn, M. C. Beard, V. Blum, and J. M. Luther, The structural origin of chiroptical properties in perovskite nanocrystals with chiral organic ligands, *Adv. Funct. Mater.* **32**, 2200454 (2022).
- [18] G. Grancini and M. K. Nazeeruddin, Dimensional tailoring of hybrid perovskites for photovoltaics, *Nat. Rev. Mater.* **4**, 4 (2019).



- [19] Y. Lekina and Z. X. Shen, Excitonic states and structural stability in two-dimensional hybrid organic-inorganic perovskites, *J. Sci.: Adv. Mater. Devices* **4**, 189 (2019).
- [20] T. Zhou, H. Lai, T. Liu, D. Lu, X. Wan, X. Zhang, Y. Liu, and Y. Chen, Highly efficient and stable solar cells based on crystalline oriented 2D/3D hybrid perovskite, *Adv. Mater.* **31**, 1901242 (2019).
- [21] B. Saparov and D. B. Mitzi, Organic-inorganic perovskites: structural versatility for functional materials design, *Chem. Rev.* **116**, 4558 (2016).
- [22] A. Rao and R. H. Friend, Harnessing singlet exciton fission to break the Shockley-Queisser limit, *Nat. Rev. Mater.* **2**, 17063 (2017).
- [23] R. D. Pensack, A. J. Tilley, S. R. Parkin, T. S. Lee, M. M. Payne, D. Gao, A. A. Jahnke, D. G. Oblinsky, P.-F. Li, J. E. Anthony, D. S. Seferos, and G. D. Scholes, Exciton delocalization drives rapid singlet fission in nanoparticles of acene derivatives, *J. Am. Chem. Soc.* **137**, 6790 (2015).
- [24] M. Braun and W. Frey, Crystal structure of bis(2-naphthylmethylammonium) lead tetrachloride,  $(C_{11}H_9NH_3)_2PbCl_4$ , *Z. Kristallogr. New Cryst. Struct.* **214**, 333 (1999).
- [25] M. Braun and W. Frey, Crystal structure of bis(2-anthrylmethylammonium) lead tetrachloride,  $(C_{15}H_{11}NH_3)_2PbCl_4$ , *Z. Kristallogr. New Cryst. Struct.* **214**, 335 (1999).
- [26] K. Du, Q. Tu, X. Zhang, Q. Han, J. Liu, S. Zauscher, and D. B. Mitzi, Two-dimensional lead(II) halide-based hybrid perovskites templated by acene alkylamines: Crystal structures, optical properties, and piezoelectricity, *Inorg. Chem.* **56**, 9291 (2017).
- [27] A. R. Bowman, S. D. Stranks, and B. Monserrat, Investigation of singlet fission-halide perovskite interfaces, *Chem. Mater.* **34**, 4865 (2022).
- [28] M. Braun and W. Frey, Crystal structure of bis(benzylammonium) lead tetrachloride,  $(C_7H_7NH_3)_2PbCl_4$ , *Z. Kristallogr. New Cryst. Struct.* **214**, 331 (1999).
- [29] E. I. Rashba and V. I. Sheka, Symmetry of energy bands in crystals of wurtzite type: II. Symmetry of bands with spin-orbit interaction included, *Fiz. Tverd. Tela: Collected Papers* **2**, 162 (1959), English translation published as supplementary material to G. Bihlmayer, O. Rader, and R. Winkler, Focus on the Rashba effect, *New J. Phys.* **17**, 050202 (2015).
- [30] X. Zhang, Q. Liu, J.-W. Luo, A. J. Freeman, and A. Zunger, Hidden spin polarization in inversion-symmetric bulk crystals, *Nat. Phys.* **10**, 387 (2014).
- [31] M. Jungfleisch, W. Zhang, R. Winkler, and A. Hoffmann, Spin-orbit torques and spin dynamics, in *Spin Physics in Semiconductors* (Springer, New York, 2017), pp. 355–385.
- [32] G. Long, C. Jiang, R. Sabatini, Z. Yang, M. Wei, L. N. Quan, Q. Liang, A. Rasmita, M. Askerka, G. Walters, X. Gong, J. Xing, X. Wen, R. Quintero-Bermudez, H. Yuan, G. Xing, X. R. Wang, D. Song, O. Voznyy, M. Zhang *et al.*, Spin control in reduced-dimensional chiral perovskites, *Nat. Photonics* **12**, 528 (2018).
- [33] W. E. Estes, D. B. Losee, and W. E. Hatfield, The magnetic properties of several quasi two-dimensional Heisenberg layer compounds: A new class of ferromagnetic insulators involving halocuprates, *J. Chem. Phys.* **72**, 630 (1980).
- [34] R. D. Willett, Structures of the antiferrodistortive layer perovskites bis(phenethylammonium) tetrahalocuprate(II), halo =  $Cl^-$ ,  $Br^-$ , *Acta Crystallogr. C: Cryst. Struct. Commun.* **46**, 565 (1990).
- [35] J. Calabrese, N. L. Jones, R. L. Harlow, N. Herron, D. L. Thorn, and Y. Wang, Preparation and characterization of layered lead halide compounds, *J. Am. Chem. Soc.* **113**, 2328 (1991).
- [36] X. Hong, T. Ishihara, and A. V. Nurmikko, Dielectric confinement effect on excitons in  $PbI_4$ -based layered semiconductors, *Phys. Rev. B* **45**, 6961 (1992).
- [37] G. Papavassiliou and I. Koutselas, Structural, optical and related properties of some natural three- and lower-dimensional semiconductor systems, *Synth. Met.* **71**, 1713 (1995).
- [38] N. K. Nobuaki Kitazawa, Compositional modulation of two-dimensional layered perovskite  $(RNH_3)_2Pb(Cl, Br, I)_4$  and its optical properties, *Jpn. J. Appl. Phys.* **35**, 6202 (1996).
- [39] N. K. Nobuaki Kitazawa, Optical absorption and photoluminescence properties of  $Pb(I, Br)$ -based two-dimensional layered perovskite, *Jpn. J. Appl. Phys.* **36**, 2272 (1997).
- [40] M. Braun, W. Tuffentsammer, H. Wachtel, and H. Wolf, Tailoring of energy levels in lead chloride based layered perovskites and energy transfer between the organic and inorganic planes, *Chem. Phys. Lett.* **303**, 157 (1999).
- [41] D. B. Mitzi, C. D. Dimitrakopoulos, and L. L. Kosbar, Structurally tailored organic-inorganic perovskites: Optical properties and solution-processed channel materials for thin-film transistors, *Chem. Mater.* **13**, 3728 (2001).
- [42] C. R. Kagan, D. B. Mitzi, and C. D. Dimitrakopoulos, Organic-inorganic hybrid materials as semiconducting channels in thin-film field-effect transistors, *Science* **286**, 945 (1999).
- [43] K. Ema, M. Inomata, Y. Kato, H. Kunugita, and M. Era, Nearly Perfect Triplet-Triplet Energy Transfer from Wannier Excitons to Naphthalene in Organic-Inorganic Hybrid Quantum-Well Materials, *Phys. Rev. Lett.* **100**, 257401 (2008).
- [44] R. Li, C. Yi, R. Ge, W. Zou, L. Cheng, N. Wang, J. Wang, and W. Huang, Room-temperature electroluminescence from two-dimensional lead halide perovskites, *Appl. Phys. Lett.* **109**, 151101 (2016).
- [45] J. P. Perdew, K. Burke, and M. Ernzerhof, Generalized Gradient Approximation Made Simple, *Phys. Rev. Lett.* **77**, 3865 (1996).
- [46] A. Tkatchenko and M. Scheffler, Accurate Molecular Van Der Waals Interactions from Ground-State Electron Density and Free-Atom Reference Data, *Phys. Rev. Lett.* **102**, 073005 (2009).
- [47] J. Heyd, G. E. Scuseria, and M. Ernzerhof, Hybrid functionals based on a screened Coulomb potential, *J. Chem. Phys.* **118**, 8207 (2003).
- [48] J. Heyd, G. E. Scuseria, and M. Ernzerhof, Erratum “Hybrid functionals based on a screened coulomb potential” [*J. Chem. Phys.* 118, 8207 (2003)], *J. Chem. Phys.* **124**, 219906 (2006).
- [49] W. P. Huhn and V. Blum, One-hundred-three compound band-structure benchmark of post-self-consistent spin-orbit coupling treatments in density functional theory, *Phys. Rev. Mater.* **1**, 033803 (2017).
- [50] M. K. Jana, R. Song, H. Liu, D. R. Khanal, S. M. Janke, R. Zhao, C. Liu, Z. V. Vardeny, V. Blum, and D. B. Mitzi, Organic-to-inorganic structural chirality transfer in a 2D hybrid perovskite and impact on Rashba-Dresselhaus spin-orbit coupling, *Nat. Commun.* **11**, 4699 (2020).
- [51] M. K. Jana, R. Song, Y. Xie, R. Zhao, P. C. Sercel, V. Blum, and D. B. Mitzi, Structural descriptor for enhanced spin-splitting in 2D hybrid perovskites, *Nat. Commun.* **12**, 4982 (2021).
- [52] G. C. Papavassiliou, G. A. Mousdis, C. P. Raptopoulou, and A. Terzis, Preparation and characterization of

- [C<sub>6</sub>H<sub>5</sub>CH<sub>2</sub>NH<sub>3</sub>]<sub>2</sub>PbI<sub>4</sub>, [C<sub>6</sub>H<sub>5</sub>CH<sub>2</sub>CH<sub>2</sub>SC(NH<sub>2</sub>)<sub>2</sub>]<sub>3</sub>PbI<sub>5</sub> and [C<sub>10</sub>H<sub>7</sub>CH<sub>2</sub>NH<sub>3</sub>]<sub>3</sub>PbI<sub>3</sub> organic-inorganic hybrid compounds, *Z. Naturforsch. B: J. Chem. Sci.* **54**, 1405 (1999).
- [53] V. Blum, R. Gehrke, F. Hanke, P. Havu, V. Havu, X. Ren, K. Reuter, and M. Scheffler, *Ab initio* molecular simulations with numeric atom-centered orbitals, *Comput. Phys. Commun.* **180**, 2175 (2009).
- [54] V. Havu, V. Blum, P. Havu, and M. Scheffler, Efficient integration for all-electron electronic structure calculation using numeric basis functions, *J. Comput. Phys.* **228**, 8367 (2009).
- [55] A. C. Ihrig, J. Wieferink, I. Y. Zhang, M. Ropo, X. Ren, P. Rinke, M. Scheffler, and V. Blum, Accurate localized resolution of identity approach for linear-scaling hybrid density functionals and for many-body perturbation theory, *New J. Phys.* **17**, 093020 (2015).
- [56] S. V. Levchenko, X. Ren, J. Wieferink, R. Johanni, P. Rinke, V. Blum, and M. Scheffler, Hybrid functionals for large periodic systems in an all-electron, numeric atom-centered basis framework, *Comput. Phys. Commun.* **192**, 60 (2015).
- [57] X. Ren, P. Rinke, V. Blum, J. Wieferink, A. Tkatchenko, A. Sanfilippo, K. Reuter, and M. Scheffler, Resolution-of-identity approach to Hartree-Fock, hybrid density functionals, RPA, MP2 and *GW* with numeric atom-centered orbital basis functions, *New J. Phys.* **14**, 053020 (2012).
- [58] See Supplemental Material at <http://link.aps.org/supplemental/10.1103/PhysRevMaterials.7.084601> for further construction details of initial structures for local energy minimization; summary of total energies and visualizations of input and relaxed geometries for all compounds; illustration of the real-space unit cell and of the Brillouin zone geometry used for band structure calculations; spin textures calculated for PMA and NMA based compounds; hydrogen bond patterns of exemplary noncentrosymmetric and centrosymmetric compounds; and listings of lattice parameters and atomic positions for fully relaxed, lowest-energy predicted structures of all compounds considered in this paper.
- [59] C. Liu, W. Huhn, K.-Z. Du, A. Vazquez-Mayagoitia, D. Dirkes, W. You, Y. Kanai, D. B. Mitzi, and V. Blum, Tunable Semiconductors: Control over Carrier States and Excitations in Layered Hybrid Organic-Inorganic Perovskites, *Phys. Rev. Lett.* **121**, 146401 (2018).
- [60] W. A. Dunlap-Shohl, E. T. Barraza, A. Barrette, S. Dovletgeldi, G. Findik, D. J. Dirkes, C. Liu, M. K. Jana, V. Blum, W. You, K. Gundogdu, A. D. Stiff-Roberts, and D. B. Mitzi, Tunable internal quantum well alignment in rationally designed oligomer-based perovskite films deposited by resonant infrared matrix-assisted pulsed laser evaporation, *Mater. Horiz.* **6**, 1707 (2019).
- [61] M. K. Jana, S. M. Janke, D. J. Dirkes, S. Dovletgeldi, C. Liu, X. Qin, K. Gundogdu, W. You, V. Blum, and D. B. Mitzi, Direct-bandgap 2D silver-bismuth iodide double perovskite: The structure-directing influence of an oligothiophene spacer cation, *J. Am. Chem. Soc.* **141**, 7955 (2019).
- [62] M. K. Jana, C. Liu, S. Lidin, D. J. Dirkes, W. You, V. Blum, and D. B. Mitzi, Resolving rotational stacking disorder and electronic level alignment in a 2D oligothiophene-based lead iodide perovskite, *Chem. Mater.* **31**, 8523 (2019).
- [63] Y. Gao, E. Shi, S. Deng, S. B. Shiring, J. M. Snaider, C. Liang, B. Yuan, R. Song, S. M. Janke, A. Liebman-Pelaez, P. Yoo, M. Zeller, B. W. Boudouris, P. Liao, C. Zhu, V. Blum, Y. Yu, B. M. Savoie, L. Huang, and L. Dou, Molecular engineering of organic-inorganic hybrid perovskites quantum wells, *Nat. Chem.* **11**, 1151 (2019).
- [64] N. E. Wright, X. Qin, J. Xu, L. L. Kelly, S. P. Harvey, M. F. Toney, V. Blum, and A. D. Stiff-Roberts, Influence of annealing and composition on the crystal structure of mixed-halide, Ruddlesden-Popper perovskites, *Chem. Mater.* **34**, 3109 (2022).
- [65] H. Lu, G. Koknat, Y. Yao, J. Hao, X. Qin, C. Xiao, R. Song, F. Merz, M. Rampp, S. Kokott, C. Carbogno, T. Li, G. Teeter, M. Scheffler, J. J. Berry, D. B. Mitzi, J. L. Blackburn, V. Blum, and M. C. Beard, Electronic impurity doping of a 2D hybrid lead iodide Perovskite by Bi and Sn, *PRX Energy* **2**, 023010 (2023).
- [66] M. Rossi, S. Chutia, M. Scheffler, and V. Blum, Validation challenge of density-functional theory for peptides—Example of Ac-Phe-Ala<sup>5</sup>-LysH<sup>+</sup>, *J. Phys. Chem. A* **118**, 7349 (2014).
- [67] F. Schubert, M. Rossi, C. Baldauf, K. Pagel, S. Warnke, G. von Helden, F. Filsinger, P. Kupser, G. Meijer, M. Salwiczek, B. Koksche, M. Scheffler, and V. Blum, Exploring the conformational preferences of 20-residue peptides in isolation: Ac-Ala<sub>19</sub>-Lys + H<sup>+</sup> vs. Ac-Lys-Ala<sub>19</sub> + H<sup>+</sup> and the current reach of DFT, *Phys. Chem. Chem. Phys.* **17**, 7373 (2015).
- [68] R. Zhao, V. W.-z. Yu, K. Zhang, Y. Xiao, Y. Zhang, and V. Blum, Quasi-four-component method with numeric atom-centered orbitals for relativistic density functional simulations of molecules and solids, *Phys. Rev. B* **103**, 245144 (2021).
- [69] A. V. Krukau, O. A. Vydrov, A. F. Izmaylov, and G. E. Scuseria, Influence of the exchange screening parameter on the performance of screened hybrid functionals, *J. Chem. Phys.* **125**, 224106 (2006).
- [70] M. A. L. Marques, J. Vidal, M. J. T. Oliveira, L. Reining, and S. Botti, Density-based mixing parameter for hybrid functionals, *Phys. Rev. B* **83**, 035119 (2011).
- [71] J. H. Skone, M. Govoni, and G. Galli, Nonempirical range-separated hybrid functionals for solids and molecules, *Phys. Rev. B* **93**, 235106 (2016).
- [72] S. Kim, M. Lee, C. Hong, Y. Yoon, H. An, D. Lee, W. Jeong, D. Yoo, Y. Kang, Y. Youn, and S. Han, A band-gap database for semiconducting inorganic materials calculated with hybrid functional, *Sci. Data* **7**, 387 (2020).
- [73] M. Steger, S. M. Janke, P. C. Sercel, B. W. Larson, H. Lu, X. Qin, V. W.-z. Yu, V. Blum, and J. L. Blackburn, On the optical anisotropy in 2D metal-halide perovskites, *Nanoscale* **14**, 752 (2022).
- [74] S. M. Janke, M. B. Qarai, V. Blum, and F. C. Spano, Frenkel-Holstein Hamiltonian applied to absorption spectra of quaterthiophene-based 2D hybrid organic-inorganic perovskites, *J. Chem. Phys.* **152**, 144702 (2020).
- [75] M. R. Filip, D. Y. Qiu, M. Del Ben, and J. B. Neaton, Screening of excitons by organic cations in quasi-two-dimensional organic-inorganic lead-halide perovskites, *Nano Lett.* **22**, 4870 (2022).
- [76] D. Seyitliyev, X. Qin, M. K. Jana, S. M. Janke, X. Zhong, W. You, D. B. Mitzi, V. Blum, and K. Gundogdu, Coherent phonon-induced modulation of charge transfer in 2D hybrid perovskites, *Adv. Funct. Mater.* **33**, 2213021 (2023).
- [77] Q. Cao, R. Song, C. C. S. Chan, Z. Wang, P. Y. Wong, K. S. Wong, V. Blum, and H. Lu, Chiral perovskite nanoplatelets with tunable circularly polarized luminescence in the strong confinement regime, *Adv. Opt. Mater.* **11**, 2203125 (2023).

- [78] D. B. Mitzi, K. Chondroudis, and C. R. Kagan, Design, structure, and optical properties of organic-inorganic perovskites containing an oligothiophene chromophore, *Inorg. Chem.* **38**, 6246 (1999).
- [79] V. K. Thorsmølle, R. D. Averitt, J. Demsar, D. L. Smith, S. Tretiak, R. L. Martin, X. Chi, B. K. Crone, A. P. Ramirez, and A. J. Taylor, Morphology Effectively Controls Singlet-Triplet Exciton Relaxation and Charge Transport in Organic Semiconductors, *Phys. Rev. Lett.* **102**, 017401 (2009).
- [80] M. K. Gish, N. A. Pace, G. Rumbles, and J. C. Johnson, Emerging design principles for enhanced solar energy utilization with singlet fission, *J. Phys. Chem. C* **123**, 3923 (2019).
- [81] S. M. Janke, M. Rossi, S. V. Levchenko, S. Kokott, M. Scheffler, and V. Blum, Pentacene and tetracene molecules and films on H/Si(111): level alignment from hybrid density functional theory, *Electron. Struct.* **2**, 035002 (2020).
- [82] M. Kepenekian, R. Robles, C. Katan, D. Saporì, L. Pedesseau, and J. Even, Rashba and Dresselhaus effects in hybrid organic-inorganic perovskites: From basics to devices, *ACS Nano* **9**, 11557 (2015).
- [83] [https://materials.hybrid3.duke.edu/materials/dataset/<dataset\\_index>](https://materials.hybrid3.duke.edu/materials/dataset/<dataset_index>). The <dataset\_index> values of the 12 predicted geometries are 2169, 2180, 2182, 2184, 2186, 2188, 2191, 2193, 2195, 2197, 2199, and 2201. The <dataset\_index> values of the 12 band structures are 2173, 2181, 2183, 2185, 2187, 2189, 2192, 2194, 2196, 2198, 2200, and 2202.
- [84] <https://nomad-lab.eu/prod/v1/gui/user/uploads/upload/id/gECchNEpTO2JkJd98L83YA>.
- [85] [https://github.com/Ruyi-Song/Oligoacene\\_DFT\\_2023](https://github.com/Ruyi-Song/Oligoacene_DFT_2023).